

Bifurcation sequences in the secular 3D planetary 3-Body problem: a geometric approach

Rita Mastroianni

Advanced Concept Team, European Space Agency, European Space Technology and Research Centre
Keplerlaan 1, 2201 AZ Noordwijk

Antonella Marchesiello

Department of Applied Mathematics, Faculty of Information Technology, Czech Technical University in Prague,
Thákurova 9, 160 00 Prague

Christos Efthymiopoulos

Dipartimento di Matematica “Tullio Levi-Civita”, Università degli Studi di Padova,
via Trieste 63, 35121 Padova,

Giuseppe Pucacco

Dipartimento di Fisica, Università degli Studi di Roma “Tor Vergata”,
via della Ricerca Scientifica 1, 00133 Roma,

e-mails: rita.mastroianni@esa.int, marchant@fit.cvut.cz
cefthym@math.unipd.it, pucacco@roma2.infn.it

Abstract

We implement the geometric method proposed in ([7], [3], [12]) to analytically predict the sequence of bifurcations leading to a change of stability and/or the appearance of new periodic orbits in the secular 3D planetary three body problem. Stemming from the analysis in [13], we examine various normal form models as regards the extent to which they lead to a phase space dynamics qualitatively similar as that in the complete system. For fixed total angular momentum, the phase space in Hopf variables is the 3D sphere, and the complete sequence of bifurcations of new periodic orbits can be recovered through formulas yielding the tangencies or degenerate intersections between the sphere and the surfaces of a constant second integral of motion of the normal form flow. In particular, we find the critical values of the second integral giving rise to pitchfork and saddle-node bifurcations of new periodic orbits in the system. This analysis renders possible to predict the most important structural changes in the phase space, as well as the emergence of new possible stable periodic planetary orbital configurations which can take place as the mutual inclination between the two planets is allowed to increase.

1 Introduction

A classical problem of Celestial Mechanics is the *planetary three-body problem*, which deals with the motion of two planets of non-negligible mass under the gravitational attraction of a star, and including the gravitational perturbation of each planet on the other. In Poincaré heliocentric canonical variables,

the problem is defined by the Hamiltonian

$$\mathcal{H}(\mathbf{r}_2, \mathbf{r}_3, \mathbf{p}_2, \mathbf{p}_3) = \frac{\mathbf{p}_2^2}{2m_2} - \frac{\mathcal{G}m_0m_2}{r_2} + \frac{\mathbf{p}_3^2}{2m_3} - \frac{\mathcal{G}m_0m_3}{r_3} + \frac{(\mathbf{p}_2 + \mathbf{p}_3)^2}{2m_0} - \frac{\mathcal{G}m_2m_3}{|\mathbf{r}_2 - \mathbf{r}_3|}, \quad (1)$$

where $m_0 \gg m_2, m_3$. The parameter m_0 represents the mass of the star, and $m_i, \mathbf{p}_i, \mathbf{r}_i, i = 2, 3$ are the masses, barycentric momenta and heliocentric position vectors of the two planets, with $r_i = |\mathbf{r}_i|$. We use the numbering (2,3) instead of (1,2) for the two planets, to have continuity with the notation of the work [13] which is the starting point whereby departs our analysis in the present paper.

The historical importance of the planetary three body problem in the conceptual growth of dynamical systems' theory in general cannot be overemphasized. Stemming from Laplace and Lagrange's investigations on the 'secular' (long-term) evolution of the planetary orbits in our own solar system ([8], [9]), the model was shown by Poincaré to serve as an archetype for the development of key ideas in dynamical systems, including the importance of periodic orbits in sculpting the phase-space structure, as well as the concepts of (near-)integrability and chaos ([17]).

In recent years, new interest in the problem has emerged owing to its close relevance to understanding planetary motions in *extrasolar* planetary systems. We refer the reader to the introduction in [13] for an extended literature review. Most recent studies stem from the planar case, i.e., where the orbits of all three bodies are co-planar. A basic known configuration of planetary orbits in such systems is the one of *apsidal corotation resonance* (ACR). In this configuration, the two planets move in osculating Keplerian ellipses whose pericenters undergo precession both with the same 'secular' (i.e., slow) frequency, remaining always either anti-aligned (hereafter 'state A') or always aligned ('state B'). Mathematically, the ACR states are periodic orbits corresponding to fixed points of the *secular Hamiltonian* of the system (see, for example, [10], [1], [11]). This is an integrable Hamiltonian produced from the Hamiltonian (1) taking the restriction to co-planar orbits, and averaging with respect to the planetary mean anomalies (see section 2).

While the planar secular planetary three body problem is well understood, several of its phase space features are already non-trivial and give rise to substantial complication in the analysis when passing from the 2D to the full 3D problem. In the latter, the planetary orbits are allowed to have non-zero mutual inclination, whose value becomes an additional parameter of the problem. Several planetary systems have been observed in a state of mutual inclination of several degrees (see [15] for a review). The main change from 2D to the 3D case is that the 3D secular Hamiltonian is *non-integrable*. After performing Jacobi reduction of the nodes, the 3D Hamiltonian is reduced to one with three degrees of freedom (DOF). The conservation of the total angular momentum leads to the existence of one global invariant besides the energy, namely the *Angular Momentum Deficit*

$$\text{AMD} = L_2 + L_3 - L_z \quad . \quad (2)$$

In Eq. (2) L_2, L_3 are the angular momenta of the circular orbits of semi-major axes a_2, a_3 equal to those of the two planets, and L_z the modulus of the total angular momentum normal to the system's Laplace plane. The lack of a third global integral implies that the system can in principle admit also chaotic solutions. As shown in the recent work [13], chaotic motions actually occupy a substantial volume in phase space as the mutual inclination of the two planets approaches the critical limit of birth of the so-called 'Lidov-Kozai' regime, where the configuration with one of the two planets in circular orbit changes stability character, turning from stable to unstable.

On the other hand, numerical investigations (see [13] and references therein, as well as section 2 below) show that the phase space of 3D secular motions acquires a rich structure at levels of the

mutual inclination well before the Lidov-Kozai regime. Our focus in the present paper is in the *near-integrable regime* arising at moderate values of the mutual inclination. Numerical experiments show that, while regular, the structure of the phase space in this regime exhibits a substantial departure from the structure of the phase space in the corresponding planar case. The main difference regards the kind of periodic orbits which represent stable possible orbital configurations for the two planets in the two cases. Most notably, in the 3D case we witness the birth of a rich variety of new possible periodic states with features quite distinct from those of the ACR states of the planar problem. Our purpose is to show that such states can be efficiently predicted and/or classified through an analysis of the *sequences of bifurcations* of periodic orbits, which stem from the ACR states (A or B) as we gradually increase the level of mutual orbital inclination. More specifically, fixing a choice of values of the star's and planets' masses (m_0, m_2, m_3) , as well as the planets' heliocentric semi-major axes (a_2, a_3) , and gradually increasing the level of mutual inclination of the orbits, we numerically observe the emergence of a certain sequence of bifurcations. This can be visualised through numerical phase portraits (surfaces of section) plotted in suitably defined Poincaré variables. Altering then the initial parameters m_i and a_i , and repeating the study, we observe that we are led to the possibility of various distinct sequences of bifurcations, some examples of which are seen in the sequence of phase portraits of figures 17 and 18 of [13]. As shown below, all such sequences belong to a class consistent with the general topological features of the phase space of the dynamical system here discussed. Our goal then becomes to give an analytical method to predict which particular sequence of bifurcations will emerge as a function of the model's parameters (m_i, a_i) and the value of the system's AMD. On physical ground, this means to predict and classify the most important possible orbital configurations (besides the ACRs) to which a planetary system with substantial level of mutual inclination can settle after its formation.

The main steps of the geometric method here implemented to achieve these goals can be summarized as follows: as a preliminary step, in *Section 2* we follow the formalism introduced in [13] to arrive at a starting 3D secular Hamiltonian model of a given system with fixed AMD. This is written as

$$\mathcal{H}_{sec} = \mathcal{H}_{planar}(\mathbf{X}, \mathbf{Y}) + \mathcal{H}_{space}(\mathbf{X}, \mathbf{Y}; \text{AMD}) \quad . \quad (3)$$

In Eq. (3), (\mathbf{X}, \mathbf{Y}) are Poincaré canonical variables for the two planets $(X_2, Y_2), (X_3, Y_3)$, which scale nearly linearly with the planets' eccentricities. The Hamiltonian \mathcal{H}_{planar} admits as a second integral the quantity

$$\sigma_0 = (X_2^2 + Y_2^2 + X_3^2 + Y_3^2)/2. \quad (4)$$

Passing, then, to the 3D case, several integrable models formally similar to \mathcal{H}_{planar} can be constructed, stemming from different (multipolar or in the order of the orbital eccentricities) truncations of the full 3D Hamiltonian \mathcal{H}_{sec} . To illustrate all aspects of the geometric method here implemented, in the following sections we focus on three different integrable models of such type.

i) A basic first model is given by the Hamiltonian

$$\mathcal{H}_{int} = \mathcal{H}_{planar} + \mathcal{H}_{0,space} \quad (5)$$

where $\mathcal{H}_{0,space}$ stems from the decomposition $\mathcal{H}_{space} = \mathcal{H}_{0,space} + \mathcal{H}_{1,space}$, such that $\mathcal{H}_{0,space}$ also admits σ_0 as a second integral.

ii) Rewriting the Hamiltonian as

$$\mathcal{H}_{sec} = \mathcal{H}_{int}(\mathbf{X}, \mathbf{Y}) + \mathcal{H}_{1,space}(\mathbf{X}, \mathbf{Y}; \text{AMD}) \quad , \quad (6)$$

and using canonical perturbation theory with Lie series (see subsection 4.2), we are led to our second integrable model, i.e., the *secular normal form*

$$\mathcal{H}_{int}^{(1)} = \mathcal{H}_{int} + \frac{1}{2} \langle \{\mathcal{H}_{1,space}, \chi\} \rangle . \quad (7)$$

In (7), χ is a Lie generating function acting to normalize the Hamiltonian (6) with respect to all terms of $\mathcal{H}_{1,space}$ not ‘in normal form’ (see subsection 4.2), and $\{\cdot, \cdot\}$ denotes the Poisson bracket operation. The averaging $\langle \cdot \rangle$ in the last term of Eq. (7) means to eliminate from $\{\mathcal{H}_{1,space}, \chi\}$ all the terms not in normal form.

iii) Our third model considered, $\tilde{\mathcal{H}}_{int}^{(N_P=3, N_{bk}=4)}$, is similar to the secular normal form $\mathcal{H}_{int}^{(1)}$, but obtained within the framework of the octupole approximation of the initial Hamiltonian truncated up to fourth order in the orbital eccentricities. Our interest in such a model, which becomes precise in cases of so-called ‘hierarchical’ systems (planets in nearly circular orbits with $a_2/a_3 \ll 1$), is motivated by the simplicity in the form of the Hamiltonian, which allows for analytical formulas to be arrived at regarding the dependence of the sequence of bifurcations on the system’s parameters.

Focusing, now, on the above three examples of integrable models approximating the 3D secular dynamics, we implement the geometric method exposed in detail in *Section 3* to obtain theoretical predictions for the sequences of bifurcations of periodic orbits arising in each model. New periodic orbits appear stemming from either of the ACR modes A or B, through both saddle-node and pitchfork bifurcations. The sequences are parameterized altering the values of each of the integrals of the energy \mathcal{E} and angular momentum σ_0 . The method relies on the use of suitable Hopf variables $\sigma_1, \sigma_2, \sigma_3$ defined so that, for fixed σ_0 , the corresponding reduced manifold in phase space is the 3-sphere $\sigma_1^2 + \sigma_2^2 + \sigma_3^2 = \sigma_0^2$. All quasi-periodic motions of the system are represented by the curves of transverse intersections of the the 2D surfaces of constant energy (e.g. $\mathcal{H}_{int}(\sigma_0, \sigma_1, \sigma_3) = \mathcal{E}$) with a sphere of fixed σ_0 . All periodic orbits of the system can then be classified in terms of two different kinds of geometric connections between constant energy surfaces and the spheres of different radii σ_0 : i) tangencies, and ii) transverse intersections, where the constant energy condition leads to a surface of degenerate form. Section 3 makes a systematic classification of these cases, the corresponding type of stability of the resulting periodic orbits, as well as the various possibilities for the resulting sequences of bifurcations, depending on the chosen integrable model. Whenever possible, we also provide the corresponding analytical formulas pertinent to the above analysis.

To verify the validity of the formulas deduced in section 3, *Section 4* implements the method to each of the models \mathcal{H}_{int} , $\mathcal{H}_{int}^{(1)}$, or $\tilde{\mathcal{H}}_{int}^{(N_P=3, N_{bk}=4)}$. Besides showing the ability of the method to predict the correct sequence of bifurcations observed in each model, a key result is that we find that even small differences in the chosen model can lead to drastic differences as regards the observed sequence of bifurcations. We explain the geometric origin of such differences. Comparing to the initial non-integrable Hamiltonian (Eq. (3)), we find that the model $\mathcal{H}_{int}^{(1)}$, which represents a higher order normal form for the secular Hamiltonian, yields also the best predictions as regards both the correct thresholds in parameter values and the form of the sequence of bifurcations. Of course, the question of how precisely a secular normal form model can approximate the true dynamics can only be answered through case by case study, i.e, studying various cases of exoplanetary systems. While this is beyond our present scope, we stress that the method exposed in Section 3 is equally applicable to all such cases.

Section 5 gives a summary of the conclusions from the present study.

2 Hamiltonian model and numerical phase portraits

2.1 Secular Hamiltonian

As in section 2.2 of [13], we derive a secular model \mathcal{H}_{sec} for the Hamiltonian (1) by performing averaging ‘by scissors’ with respect to the fast angles. Let $(a, e, i, M, \omega, \Omega)$ be the Keplerian elements of a body (semi-major axis, eccentricity, inclination, mean anomaly, argument of the periastron, argument of the nodes). Denoting $\lambda = M + \omega + \Omega$, $\varpi = \omega + \Omega$ the mean longitude and longitude of the periastron respectively, the secular model is obtained averaging \mathcal{H} with respect to the fast angles M_2, M_3 :

$$\begin{aligned} \mathcal{H}_{sec} &= \frac{1}{4\pi^2} \int_0^{2\pi} \int_0^{2\pi} \mathcal{H}(\mathbf{r}_2, \mathbf{r}_3, \mathbf{p}_2, \mathbf{p}_3) dM_2 dM_3 \\ &= -\frac{\mathcal{G}m_0m_2}{2a_2} - \frac{\mathcal{G}m_0m_3}{2a_3} + \frac{\mathcal{G}m_2^2}{2a_2} + \frac{\mathcal{G}m_3^2}{2a_3} - \frac{\mathcal{G}m_2m_3}{a_3} + \mathcal{R}_{sec}(a_2, a_3, e_2, e_3, i_2, i_3, \omega_2, \omega_3, \Omega_2 - \Omega_3), \end{aligned} \quad (8)$$

where

$$\mathcal{R}_{sec} = \frac{1}{4\pi^2} \int_0^{2\pi} \int_0^{2\pi} -\frac{\mathcal{G}m_2m_3}{r_3} \left(-\frac{1}{2} \frac{r_2^2}{r_3^2} + \frac{3}{2} \frac{(\mathbf{r}_2 \cdot \mathbf{r}_3)^2}{r_3^4} + \dots \right) dM_2 dM_3. \quad (9)$$

Keeping only the lowest order term in the integrand of (9), proportional to $(r_2/r_3)^2$, leads to the so-called *quadrupole* approximation; the next truncation (up to terms proportional to $(r_2/r_3)^3$) is the *octupole* approximation, etc. The integrals of any multipole approximation can be computed in so-called *closed form* (i.e. without expansions in the eccentricities), by avoiding completely the series reversion of Kepler’s equation, using, instead, the change of variables $M_2 \rightarrow u_2$ (eccentric anomaly), $M_3 \rightarrow f_3$ (true anomaly).

Following, now, section 2.3 of [13], we first Jacobi-reduce the Hamiltonian (8), introducing a ‘book-keeping symbol’ which keeps track of the order of smallness in eccentricity and mutual inclination of all the terms in the Hamiltonian expansion. This leads to the decomposition:

$$\mathcal{H}_{sec}(w_2, w_3, W_2, W_3; L_z) = \mathcal{H}_{planar}(w_2 - w_3, W_2, W_3) + \mathcal{H}_{space}(w_2, w_3, W_2, W_3; L_z), \quad (10)$$

where

$$\begin{aligned} \Lambda_j &= L_j, & \lambda_j &= M_j + \omega_j + \Omega_j, \\ W_j &= L_j - G_j, & w_j &= -\omega_j, \end{aligned} \quad (11)$$

are modified Delaunay variables, with $j = 2, 3$, and

$$\begin{aligned} L_j &= m_j \sqrt{\mathcal{G}m_0 a_j}, & l_j &= M_j, \\ G_j &= L_j \sqrt{1 - e_j^2}, & g_j &= \omega_j, \\ H_j &= G_j \cos(i_j), & h_j &= \Omega_j. \end{aligned} \quad (12)$$

The spatial part \mathcal{H}_{space} can be split as $\mathcal{H}_{space} = \mathcal{H}_{0,space} + \mathcal{H}_{1,space}$, where $\mathcal{H}_{0,space}$ contains terms independent of the angles or depending trigonometrically on the difference $w_2 - w_3 = \omega_3 - \omega_2$, and $\mathcal{H}_{1,space}$ contains terms depending trigonometrically on combinations of the angles w_2, w_3 other than their difference. Then we write

$$\mathcal{H}_{sec} = \underbrace{\mathcal{H}_{planar}(w_2 - w_3, W_2, W_3) + \mathcal{H}_{0,space}(w_2 - w_3, W_2, W_3; L_z)}_{\text{Integrable part} := \mathcal{H}_{int}} + \mathcal{H}_{1,space}(w_2, w_3, W_2, W_3; L_z). \quad (13)$$

The first two terms in the above expression give rise to a 2 degrees of freedom integrable Hamiltonian

$$\mathcal{H}_{int}(w_2 - w_3, W_2, W_3; \text{AMD}) = \mathcal{H}_{planar}(w_2 - w_3, W_2, W_3) + \mathcal{H}_{0,space}(w_2 - w_3, W_2, W_3; \text{AMD}), \quad (14)$$

(where the AMD is defined as in Eq. (2)), whose second integral is $W_2 + W_3$.

2.2 Numerical phase portraits

The only exact integral of motion for the Hamiltonian \mathcal{H}_{sec} is the energy integral $\mathcal{H}_{sec}(X_2, Y_2, X_3, Y_3 = 0; \text{AMD}) = \mathcal{E}$. Exploiting the constancy of the energy, we can define a suitable Poincaré surface of section $\mathcal{P}(\mathcal{E}; \text{AMD})$ capturing all the important structural changes in the phase space under the Hamiltonian \mathcal{H}_{sec} as the energy \mathcal{E} increases. As demonstrated in [13], increasing the energy \mathcal{E} in the Jacobi-reduced Hamiltonian means orbits of higher mutual inclination at a given level of eccentricities, or higher eccentricity at a given level of mutual inclination. We define the surface of section through the relations

$$\mathcal{PS}_{\mathcal{H}_{sec}}(\mathcal{E}; \text{AMD}) = \left\{ (X_2, Y_2, X_3, Y_3) \in \mathbb{R}^4 : \mathcal{H}_{sec}(X_2, Y_2, X_3, Y_3 = 0; \text{AMD}) = \mathcal{E}, Y_3 = 0, \right. \\ \left. \dot{Y}_3 = -\frac{\partial \mathcal{H}_{sec}}{\partial X_3} \Big|_{Y_3=0} \geq 0, \cos(i_{max}) \leq \cos(i_{mut})(X_2, Y_2, X_3, Y_3 = 0; \text{AMD}) \leq 1 \right\}, \quad (15)$$

where the variables (X_j, Y_j) are Poincaré canonical coordinates and momenta related to the variables (w_j, W_j) through the canonical transformation

$$X_j = -\sqrt{2W_j} \cos(w_j), \quad Y_j = \sqrt{2W_j} \sin(w_j), \quad j = 2, 3. \quad (16)$$

The mutual inclination $i_{mut} = i_2 + i_3$ for fixed AMD is given by

$$\cos(i_{mut}) = \frac{L_z^2 - \Lambda_2^2 - \Lambda_3^2 + \Lambda_2^2 e_2^2 + \Lambda_3^2 e_3^2}{2\Lambda_2\Lambda_3\sqrt{1-e_2^2}\sqrt{1-e_3^2}} = \frac{L_z^2 - G_2^2 - G_3^2}{2G_2G_3} \quad (17)$$

where $L_z = \Lambda_2 + \Lambda_3 - \text{AMD}$. The maximum possible mutual inclination consistent with the given AMD is

$$i_{max} = \cos^{-1} \left(\frac{L_z^2 - \Lambda_2^2 - \Lambda_3^2}{2\Lambda_2\Lambda_3} \right). \quad (18)$$

The phase portrait corresponding to the Poincaré surface of section at a fixed level of energy \mathcal{E} is obtained numerically, by choosing several initial conditions $(X_2, Y_2) \in \mathcal{D}(\mathcal{E}) \subset \mathbb{R}^2$, where $\mathcal{D}(\mathcal{E})$ is the domain of permissible initial conditions consistent with the definition of the surface of section as defined in Eq. (15). Figure 1 shows an example of computation of phase portraits, referring to the mass, periods and AMD parameters as estimated for the v -Andromedæ system reported in section 2.4 of [13]. We use a model truncated at multipolar order $N_P = 5$ and of book-keeping order $N_{bk} = 12$. This essentially reproduces Figs. 5 and 9 of [13], but illustrating the surface of section in the canonical variables (X_2, Y_2) instead of their ‘physical’ analogues $(e_2 \cos(\omega_2), e_2 \sin(\omega_2))$.

Figure 1 allows to recognize one out of all in-principle possible chains of bifurcations that can emerge in 3D secular models of the type discussed above. Such models may differ in the parameters (masses and semi-major axes of the planets, value of the AMD) as well as on the truncation orders (in the multipoles and/or the orbital eccentricities and inclinations). Our aim in the next section is to

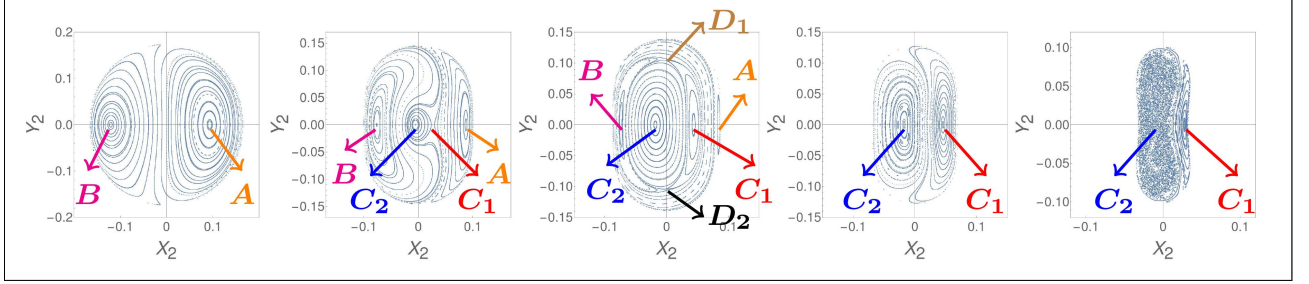


Figure 1: Poincaré surfaces of section $\mathcal{PS}_{\mathcal{H}_{sec}}(\mathcal{E}; \text{AMD})$ in the plane (X_2, Y_2) with AMD fixed and different values of energy. The surfaces of section are computed by a numerical integration of trajectories in the Hamiltonian truncated at multipolar degree $N_P = 5$, order $N_{bk} = 12$ in the eccentricities, and energies (from left to right) $\mathcal{E} = -6.77 \cdot 10^{-5}, -2.53 \cdot 10^{-5}, -1.92 \cdot 10^{-5}, -1.17 \cdot 10^{-5}, -2.61 \cdot 10^{-6}$.

provide a systematic method to predict which out of all possibilities actually takes place in a system with given parameters. In the case of Fig. 1, a quick description of the numerically obtained sequence of bifurcations is as follows: for low \mathcal{E} , i.e., nearly planar orbits (left most panel in 1) the phase portrait exhibits two stable fixed points which correspond to the ACR modes A (right fixed point) and B (left fixed point, reversed with respect to the left-right position of the same fixed points in figure 9 of [13]). In between the centers A and B we have a continuous transition of quasi-periodic orbits represented in the surface of section by closed curves surrounding either the fixed point A or B. No unstable points or separatrices exist between the stable points, while the apparent separation of the two domains is only an artifact of the projection of the phase space, whose real topology is the one of the 2-sphere (see below), to the plane (X_2, Y_2) . The second panel in Fig. 1 shows, now, the birth of the families called ‘C1’ (unstable) and ‘C2’ (stable) in [13] through a saddle-node bifurcation. The unstable orbit C1 quickly becomes stable through a pitchfork bifurcation giving rise to two ‘off-axis’ ($Y_2 \neq 0$) unstable orbits which later (as the energy \mathcal{E} increases) join each other through an inverse pitchfork bifurcation turning the left fixed point of the middle panel of Fig. 1 from stable to unstable. For still higher energy \mathcal{E} , the C2 orbit finally turns also to unstable via the ‘Lidov-Kozai’ mechanism. Note that in this last regime a large volume of the phase space is dominated by chaotic motions, hence excluded by any of the integrable models used in the sequel to approximate the flow under the complete Hamiltonian.

3 Sequences of bifurcations: geometric method of determination

3.1 Preliminary definitions. Equivalence of phase portraits

The Poincaré surfaces of section $\mathcal{PS}_{\mathcal{H}_{sec}}(\mathcal{E}; \text{AMD})$ in Fig. 1 were obtained by fixing the value of the energy \mathcal{E} and taking a set of initial conditions for each energy. Hence, every periodic orbit P yields a fixed point with coordinates $X_{2,P}(\mathcal{E}), Y_{2,P}(\mathcal{E})$, with \mathcal{E} , in general, within two limits $\mathcal{E}_{min,P} \leq \mathcal{E} \leq \mathcal{E}_{max,P}$. The energies $\mathcal{E}_{min,P}, \mathcal{E}_{max,P}$ are called the *bifurcation limits* of the periodic orbit P , while the curves $C_P = \text{graph of } X_{2,P}(\mathcal{E}), Y_{2,P}(\mathcal{E}) \text{ as a function of } \mathcal{E}$ are called characteristic curves.

Consider all possible periodic orbits $P_n, n = 1, 2, \dots$ yielding fixed points on the section $\mathcal{PS}_{\mathcal{H}_{sec}}(\mathcal{E}; \text{AMD})$ of a given character of Floquet stability S_n (with values ‘stable’ or ‘unstable’), and sorted in ascending values of \mathcal{E}_{min,P_n} . The set $\mathcal{B} \equiv \{(\mathcal{E}_{min,P_n}, \mathcal{E}_{max,P_n}, C_{P_n}, S_n), n = 1, 2, \dots\}$ is hereafter called a

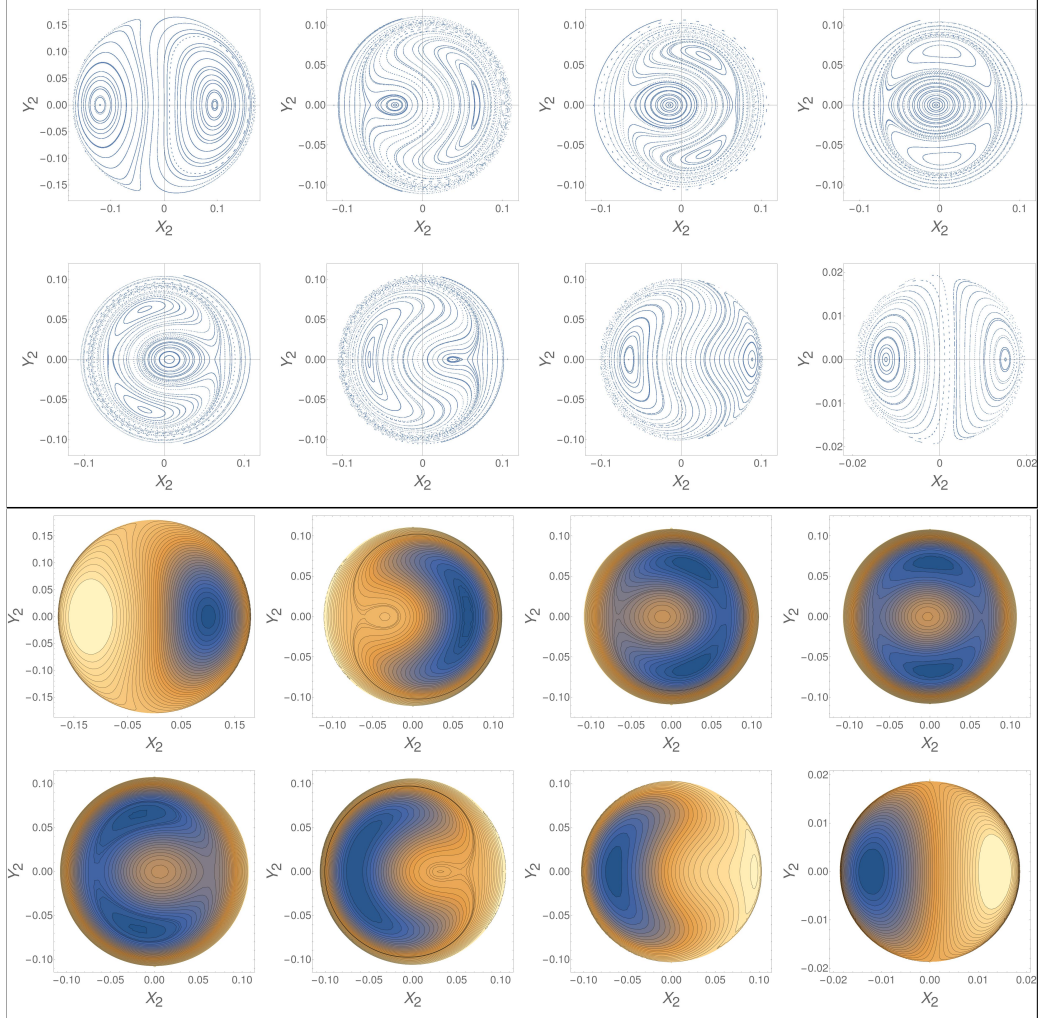


Figure 2: *Top frame:* Poincaré surfaces of section $\mathcal{PS}_{\mathcal{H}_{int}}(\mathcal{E}; \text{AMD})$ for the integrable Hamiltonian model \mathcal{H}_{int} at the values of the energies (from top to bottom, left to right) $\mathcal{E} = -6.77 \cdot 10^{-5}, -1.8 \cdot 10^{-5}, -1.74 \cdot 10^{-5}, -1.7 \cdot 10^{-5}, -1.67 \cdot 10^{-5}, -1.6 \cdot 10^{-5}, -1.43 \cdot 10^{-5}, -4.05 \cdot 10^{-7}$. *Bottom frame:* Phase portraits by contour plots $\mathcal{P}_{\mathcal{H}_{int}}(\sigma_0; \text{AMD})$ with decreasing values of σ_0 (from top to bottom, left to right) $\sigma_0 = 1.62 \cdot 10^{-2}, 6.15 \cdot 10^{-3}, 5.93 \cdot 10^{-3}, 5.85 \cdot 10^{-3}, 5.78 \cdot 10^{-3}, 5.62 \cdot 10^{-3}, 5.304 \cdot 10^{-3}, 1.74 \cdot 10^{-4}$. The two alternative representations of the phase portraits, corresponding to $\mathcal{P}_{\mathcal{Z}}(\mathcal{E})$ (top) or $\mathcal{P}_{\mathcal{Z}}(\sigma_0)$ (bottom), for $\mathcal{Z} = \mathcal{H}_{int}$, yield an equivalent bifurcation sequence.

bifurcation sequence.

The definition of a bifurcation sequence \mathcal{B} as above requires parameterizing all bifurcation limits in terms of the corresponding energies $(\mathcal{E}_{min,P_n}, \mathcal{E}_{max,P_n})$. To predict the structural changes in the corresponding phase portraits after the n -th bifurcation in the sequence, we employ integrable approximations to the dynamics, as the models \mathcal{H}_{int} , $\mathcal{H}_{int}^{(1)}$, or $\tilde{\mathcal{H}}_{int}^{(N_P=3, N_{bk}=4)}$ mentioned in the introduction. An integrable approximation \mathcal{Z} to the Hamiltonian \mathcal{H}_{sec} is defined as a Hamiltonian which i) admits σ_0 (Eq.(4)) as a second integral, and ii) has flow close to the flow of \mathcal{H}_{sec} . The closeness of the two flows can be established by appropriate norms in the functional space containing the derivatives of \mathcal{H}_{sec} and \mathcal{Z} . Let \mathcal{Z} be an integrable approximation to \mathcal{H}_{sec} . Define the family of curves

$$\begin{aligned} \mathcal{C}_{\mathcal{Z}}(\sigma_0; \mathcal{E}; \text{AMD}) = & \left\{ (X_2, Y_2) \in \mathbb{R}^2 : \mathcal{Z}(X_2, Y_2, X_3 = X_{3,+}, Y_3 = 0; \text{AMD}) = \mathcal{E}, \right. \\ & X_2^2 + Y_2^2 + X_{3,+}^2 = 2\sigma_0, \quad \dot{Y}_3 = -\frac{\partial \mathcal{Z}}{\partial X_3} \Big|_{Y_3=0, X_3=X_{3,+}} \geq 0, \\ & \left. \cos(i_{max}) \leq \cos(i_{mut})(X_2, Y_2, X_3 = X_{3,+}, Y_3 = 0; \text{AMD}) \leq 1 \right\}. \end{aligned} \quad (19)$$

A σ_0 -fixed phase portrait of \mathcal{Z} is defined by the family of curves

$$\mathcal{P}_{\mathcal{Z}}(\sigma_0) = \left\{ \mathcal{C}_{\mathcal{Z}}(\sigma_0; \mathcal{E}; \text{AMD}), \quad \mathcal{E}_L(\sigma_0, \text{AMD}) \leq \mathcal{E} \leq \mathcal{E}_R(\sigma_0, \text{AMD}) \right\}, \quad (20)$$

where the functions $\mathcal{E}_L(\sigma_0, \text{AMD}), \mathcal{E}_R(\sigma_0, \text{AMD})$ are defined by the requirement that the angular momentum deficit of the system is equal to the given value AMD (see [13] as well as the caption in Fig. 3). A \mathcal{E} -fixed phase portrait of \mathcal{Z} is defined by the family of curves

$$\mathcal{P}_{\mathcal{Z}}(\mathcal{E}) = \{ \mathcal{C}_{\mathcal{Z}}(\sigma_0; \mathcal{E}; \text{AMD}), \quad \sigma_{0,min}(\mathcal{E}, \text{AMD}) \leq \sigma_0 \leq \sigma_{0,max}(\mathcal{E}, \text{AMD}) \} \quad (21)$$

where the functions $\sigma_{0,min}(\mathcal{E}, \text{AMD}), \sigma_{0,max}(\mathcal{E}, \text{AMD})$ are defined through the inverse of the functions $\mathcal{E}_L(\sigma_0, \text{AMD}), \mathcal{E}_R(\sigma_0, \text{AMD})$.

By the above definitions the following hold:

i) \mathcal{E} -fixed phase portraits of \mathcal{Z} are equivalent to the Poincaré surfaces of section $\mathcal{PS}_{\mathcal{Z}}(\mathcal{E}; \text{AMD})$. The equivalence is demonstrated below. Since the flow of \mathcal{Z} is close to the flow of \mathcal{H}_{sec} in a suitable domain of initial conditions the phase portraits $\mathcal{P}_{\mathcal{Z}}(\mathcal{E})$ are expected to approximate as well the phase portraits of the full non-integrable Hamiltonian \mathcal{H}_{sec} , obtained through the Poincaré surfaces of section $\mathcal{PS}_{\mathcal{H}_{sec}}(\mathcal{E}; \text{AMD})$.

ii) For fixed integrable model \mathcal{Z} , the phase portraits $\mathcal{P}_{\mathcal{Z}}(\mathcal{E})$ and $\mathcal{P}_{\mathcal{Z}}(\sigma_0)$ yield an equivalent sequence of bifurcations. This is an obvious consequence of the definition of bifurcation sequence together with the fact that the sets $\mathcal{P}_{\mathcal{Z}}(\mathcal{E})$ and $\mathcal{P}_{\mathcal{Z}}(\sigma_0)$, spanning the whole permissible domain in \mathcal{E} and σ_0 (Fig.3), contain the same curves $\mathcal{C}_{\mathcal{Z}}(\sigma_0, \mathcal{E}; \text{AMD})$. An example of this equivalence is provided in Fig. 2.

Note that, due to the last property mentioned in (i), only the representation $\mathcal{P}_{\mathcal{Z}}(\mathcal{E})$ can be compared directly with the numerical phase-portraits under the full (non-integrable) Hamiltonian \mathcal{H}_{sec} . On the other hand, due to (ii), the theoretical analysis of the bifurcation sequences can be performed exploring the geometric properties of the representation $\mathcal{P}_{\mathcal{Z}}(\sigma_0)$ in suitable Hopf variables (see next subsection). The equivalence property then establishes the equality of the bifurcation sequences exhibited by either representation.

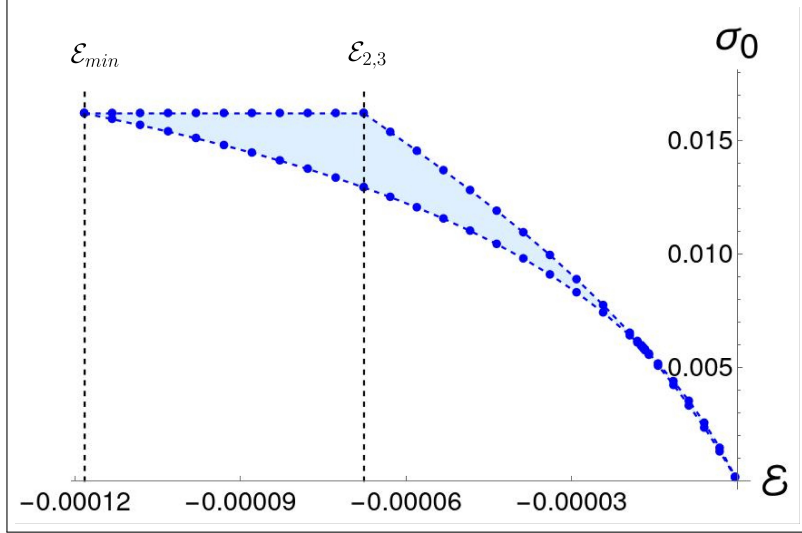


Figure 3: The permissible domain in \mathcal{E} and σ_0 consistent with a fixed value of the system's AMD. The numerical curves shown above refer to the example of the integrable model $\mathcal{Z} = \mathcal{H}_{int}$. Fixing a value of σ_0 , the two limiting curves yield the corresponding limiting energies $\mathcal{E}_L(\sigma_0)$, $\mathcal{E}_R(\sigma_0)$. Alternatively, fixing a value of the energy we obtain the limits $\sigma_{0,min}(\mathcal{E}), \sigma_{0,max}(\mathcal{E})$. The above limits can be computed analytically as explained in [13]. In summary, there exist two critical values of the energy \mathcal{E}_{min} , $\mathcal{E}_{2,3}$ such that, for any value of the energy in the interval $\mathcal{E}_{min} < \mathcal{E} < \mathcal{E}_{2,3}$, σ_0 is limited from below by a minimum value $\sigma_{0,min}(\mathcal{E})$, while the limit from above $\sigma_{0,max}$ is posed only by the globally maximum value $\sigma_{0,max} = \sigma_{0,AMD} = AMD$. The limiting values $\mathcal{E} = \mathcal{E}_{min}$ and $\mathcal{E} = \mathcal{E}_{2,3}$ correspond to the co-planar ACR orbits A (anti-aligned) and B (aligned) respectively. On the other hand, for energies larger than $\mathcal{E}_{2,3}$ there are no possible co-planar orbits, and $\sigma_{0,max}$ as well becomes a decreasing function of \mathcal{E} . Overall, as we move from left to right or top to bottom, we obtain orbits of higher mutual inclination. For the Hamiltonian \mathcal{H}_{int} (see text for parameter values) we compute the values $\mathcal{E}_{min} = -1.18 \cdot 10^{-4}$ and $\mathcal{E}_{2,3} = -6.77 \cdot 10^{-5}$ and $\sigma_{0,max} = AMD = 0.0162044$.

To demonstrate the equivalence of the phase portraits $\mathcal{P}_{\mathcal{Z}}(\mathcal{E})$ and $\mathcal{PS}_{\mathcal{Z}}(\mathcal{E}; \text{AMD})$, define the canonical transformation

$$\begin{aligned}\psi &= w_2 - w_3, & \Gamma &= \frac{W_2 - W_3}{2}, \\ \varphi &= w_2 + w_3, & J &= \frac{W_2 + W_3}{2}.\end{aligned}\quad (22)$$

The integrable Hamiltonian \mathcal{Z} in the new variables reads (apart from a constant)

$$\mathcal{Z}(\psi, \varphi, \Gamma, J) = \mathcal{Z}(\psi, \Gamma; J), \quad (23)$$

i.e., the angle φ is ignorable. In view of Eq. (23), \mathcal{Z} can be regarded as defining either the complete flow in four variables $(\psi, \varphi, \Gamma, J)$, or, alternatively, the flow a one degree of freedom Hamiltonian in the variables (ψ, Γ) , with J serving as parameter. Hence, the level curves of constant energy $\mathcal{Z}(\psi, \Gamma; J) = \mathcal{E}$ computed in the plane (ψ, Γ) for various values of the energy and keeping fixed the value of J are geometrically equivalent to the invariant curves in the Poincaré section under the complete 2-DOF flow. In particular, any closed curve γ (1-torus) in the top frame of Fig. 2 represents a 2-torus of the full flow, obtained by the product $\gamma \times$ the 1-torus defined by the solution for φ of the differential equation $\dot{\varphi} = (\partial\mathcal{Z}/\partial J)_{\psi=\psi_\gamma(t), \Gamma=\Gamma_\gamma(t)}$, where $\psi_\gamma(t), \Gamma_\gamma(t)$ is the solution of the Hamiltonian flow for the variables (ψ, Γ) along the curve γ . In the same way, any fixed point (ψ_0, Γ_0) in the same plots represents a periodic orbit $\varphi(t) = \varphi(0) + (\partial\mathcal{Z}/\partial J)_{\psi=\psi_0, \Gamma=\Gamma_0} t$ of the complete flow. Hence, the problem of the number and bifurcations of new periodic orbits in the complete 2-DOF flow is reduced to the problem of the number and bifurcations of new fixed points in the reduced 1-DOF flow.

3.2 Hopf representation of the phase space

Having established the equivalence of all kinds of phase portraits defined in the previous subsection, we now focus on the theoretical interpretation of the structural changes in the phase portraits $\mathcal{P}_{\mathcal{Z}}(\sigma_0)$ (e.g. those of Fig. 2, bottom frame), as σ_0 is altered within the established permissible domain of values. To this end, it turns convenient to express the Hamiltonian flow in terms of Hopf variables $(\sigma_1, \sigma_2, \sigma_3)$ defined by:

$$\sigma_1 = X_2 X_3 + Y_2 Y_3, \quad \sigma_2 = Y_2 X_3 - Y_3 X_2, \quad \sigma_3 = \frac{1}{2} (X_2^2 + Y_2^2 - X_3^2 - Y_3^2), \quad (24)$$

satisfying the Poisson algebra $\{\sigma_i, \sigma_j\} = -2\epsilon_{ijk}\sigma_k$, where ϵ_{ijk} is the Levi-Civita symbol and $i, j, k = 1, 2, 3$. Furthermore, we introduce the variable

$$\sigma_0 = \frac{1}{2} (X_2^2 + Y_2^2 + X_3^2 + Y_3^2) \quad (25)$$

which is a Casimir invariant of the previous algebra (all Poisson brackets $\{\sigma_i, \sigma_0\}$, $i = 1, 2, 3$, vanish). From the definition (24) it follows that

$$\begin{aligned}\sigma_1 &= 2\sqrt{J+\Gamma}\sqrt{J-\Gamma}\cos(\psi), & \sigma_2 &= -2\sqrt{J+\Gamma}\sqrt{J-\Gamma}\sin(\psi), \\ \sigma_3 &= W_2 - W_3 = 2\Gamma.\end{aligned}\quad (26)$$

We also have the relation $\sigma_0 = W_2 + W_3 = 2J$, as well as

$$\sigma_1^2 + \sigma_2^2 + \sigma_3^2 = \sigma_0^2 = 4J^2. \quad (27)$$

The latter expression implies that, for any fixed value of the constant J , the flow under any of the integrable models \mathcal{Z} approximating the Hamiltonian, represented in a Euclidean space with axes $(\sigma_1, \sigma_2, \sigma_3)$, is restricted to the 2-sphere of radius σ_0 .

Given the values of $(\sigma_1, \sigma_2, \sigma_3)$, the values of Γ , J and ψ can be computed unequivocally using the relations (26) and (27). Furthermore, the Hamiltonian \mathcal{Z} is even in the difference $w_2 - w_3$, hence it does not depend on σ_2 , i.e., $\mathcal{Z} = \mathcal{Z}(\sigma_1, \sigma_3; \sigma_0)$. Fixing a value of σ_0 (i.e. of the integral $J = \sigma_0/2$), the continuous in time phase flow under \mathcal{Z} can be expressed in the Hopf variables via the equations

$$\dot{\sigma}_1 = \{\sigma_1, \sigma_3\} \frac{\partial \mathcal{Z}}{\partial \sigma_3}, \quad \dot{\sigma}_2 = \{\sigma_2, \sigma_1\} \frac{\partial \mathcal{Z}}{\partial \sigma_1} + \{\sigma_2, \sigma_3\} \frac{\partial \mathcal{Z}}{\partial \sigma_3}, \quad \dot{\sigma}_3 = -\{\sigma_1, \sigma_3\} \frac{\partial \mathcal{Z}}{\partial \sigma_1}. \quad (28)$$

In particular, the level curves of Fig. 2 can be represented by the intersection of the constant energy surface $\mathcal{Z}(\sigma_1, \sigma_3; \sigma_0) = \mathcal{E}$ with the sphere (27). Altering the energy \mathcal{E} in the interval $\mathcal{E}_L(\sigma_0) \leq \mathcal{E} \leq \mathcal{E}_R(\sigma_0)$, while keeping $\sigma_0 = 2J$ constant yields a family of closed curves on the sphere which can be mapped to the invariant curves of the Poincaré surface of section of Fig. 2 through the relations $X_2 = -\sqrt{2(\Gamma + J)} \cos(\psi - \pi)$, $Y_2 = \sqrt{2(\Gamma + J)} \sin(\psi - \pi)$, with $\Gamma = \sigma_3/2$, $\cos \psi = \sigma_1/(\sqrt{\sigma_0^2 - \sigma_3^2})$, $\sin \psi = \sigma_2/(\sqrt{\sigma_0^2 - \sigma_3^2})$. Equivalently, keeping the energy \mathcal{E} fixed and altering σ_0 in the interval $\sigma_{0,min}(\mathcal{E}) \leq \sigma_0 \leq \sigma_{0,max}(\mathcal{E})$ allows to recover the family of all invariant curves in Fig. 2.

3.3 Geometrical representation of the sequence of bifurcations

Consider a fixed integral approximation \mathcal{Z} to the Hamiltonian \mathcal{H}_{sec} . Let

$$\mathcal{S}_{\sigma_0} = \{(\sigma_1, \sigma_2, \sigma_3) \in \mathbb{R}^3 : \sigma_1^2 + \sigma_2^2 + \sigma_3^2 = \sigma_0^2\} \quad (29)$$

be the sphere of fixed radius σ_0 and

$$\mathcal{C}_{\sigma_0, \mathcal{E}} = \{(\sigma_1, \sigma_2, \sigma_3) \in \mathbb{R}^3 : \mathcal{Z}(\sigma_0, \sigma_1, \sigma_3) = \mathcal{E}\}, \quad (30)$$

the constant energy surface in the space $(\sigma_1, \sigma_2, \sigma_3) \in \mathbb{R}^3$. By altering the parameters (σ_0, \mathcal{E}) we have three possibilities:

i) \mathcal{S}_{σ_0} and $\mathcal{C}_{\sigma_0, \mathcal{E}}$ have no common points. This corresponds to values (σ_0, \mathcal{E}) outside the permissible area by the curves of Fig. 3.

ii) \mathcal{S}_{σ_0} and $\mathcal{C}_{\sigma_0, \mathcal{E}}$ intersect transversally. This yields, in general, closed curves in the sphere \mathcal{S}_{σ_0} representing quasi-periodic orbits of the Hamiltonian \mathcal{Z} . In degenerate cases, the closed curves reduce to points representing periodic orbits of the flow under \mathcal{Z} .

iii) $\mathcal{C}_{\sigma_0, \mathcal{E}}$ arrives tangently to one or more points of \mathcal{S}_{σ_0} . The point of tangency is a periodic orbit of the flow under \mathcal{Z} .

The whole sequence of bifurcations of new fixed points as in Fig. 2 can be computed exploiting the above properties as follows: since the Hamiltonian does not depend on σ_2 , for any fixed value of σ_0 all possible kinds of intersection or tangency of the surface $\mathcal{C}_{\sigma_0, \mathcal{E}}$ with \mathcal{S}_{σ_0} can be classified through their projection to the plane $\sigma_2 = 0$. In particular, all points of tangency are along the meridian of the sphere $\mathcal{S}_{\sigma_0}^{(\sigma_2=0)}$ contained in the plane (σ_1, σ_3) with $\sigma_2 = 0$. Altering the energy in the interval $\mathcal{E}_L(\sigma_0) \leq \mathcal{E} \leq \mathcal{E}_R(\sigma_0)$ we then compute the curve $\mathcal{C}_{\sigma_0, \mathcal{E}}^{(\sigma_2=0)}$ at which the surface $\mathcal{C}_{\sigma_0, \mathcal{E}}$ intersects the same plane, for values of \mathcal{E} within the permissible limits discussed in the previous subsection. We then distinguish two cases, both satisfying the equation

$$\nabla \mathcal{Z} = \mu (\sigma_1, \sigma_2, \sigma_3) \quad (31)$$

for some $\mu \in \mathbb{R}$.

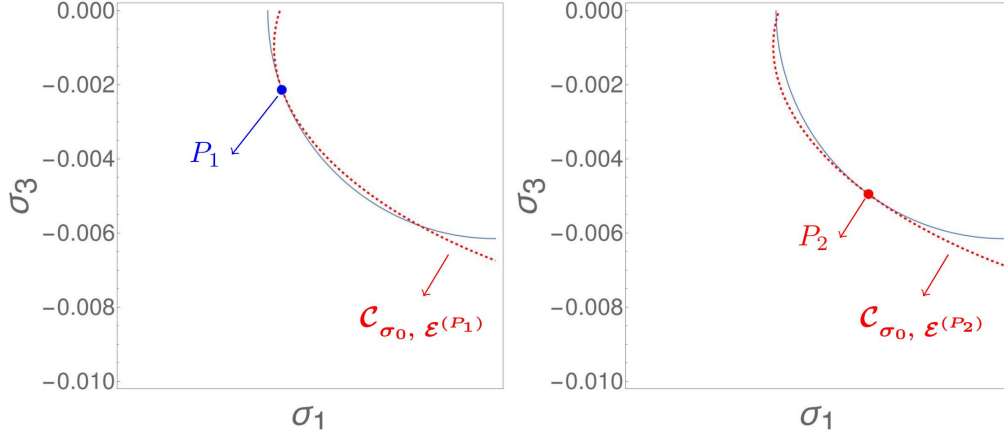


Figure 4: An example of inner tangency between \mathcal{S}_{σ_0} and $\mathcal{C}_{\sigma_0, \mathcal{E}^{(P_1)}}$ at the point P_1 (left), and outer tangency at the point P_2 (right). The example is taken from the analysis of the integrable model $\mathcal{Z} = \mathcal{H}_{int}$ (see second panel of the second row of Fig. 6, corresponding to the phase portrait $\mathcal{P}_{\mathcal{Z}}(\sigma_0)$ with $= 6.15 \cdot 10^{-3}$)).

3.3.1 Case 1: Non-degenerate tangency of \mathcal{S}_{σ_0} and $\mathcal{C}_{\sigma_0, \mathcal{E}}$

Non-degenerate tangency points of the surfaces \mathcal{S}_{σ_0} and $\mathcal{C}_{\sigma_0, \mathcal{E}}$ are contained in the curves $\mathcal{S}_{\sigma_0}^{(\sigma_2=0)}$ and $\mathcal{C}_{\sigma_0, \mathcal{E}}^{(\sigma_2=0)}$ and satisfy the condition

$$\sigma_2 = 0, \quad \nabla_{\sigma_1, \sigma_3} (\mathcal{Z})_{\sigma_2=0} \neq 0, \quad \text{rank} \begin{pmatrix} 2\sigma_1 & 2\sigma_3 \\ \frac{\partial \mathcal{Z}}{\partial \sigma_1} & \frac{\partial \mathcal{Z}}{\partial \sigma_3} \end{pmatrix} = 1, \quad (31)$$

(i.e. Eq. (31) with $\mu \neq 0$) implying

$$\sigma_2 = 0, \quad \sigma_3 \frac{\partial \mathcal{Z}}{\partial \sigma_1} = \sigma_1 \frac{\partial \mathcal{Z}}{\partial \sigma_3}. \quad (32)$$

By Eq. (32) we have that the point of tangency is a fixed point of the flow (28) since

$$\frac{\dot{\sigma}_1}{2} = \sigma_2 \frac{\partial \mathcal{Z}}{\partial \sigma_3} = 0, \quad \frac{\dot{\sigma}_2}{2} = \sigma_3 \frac{\partial \mathcal{Z}}{\partial \sigma_1} - \sigma_1 \frac{\partial \mathcal{Z}}{\partial \sigma_3} = 0, \quad \frac{\dot{\sigma}_3}{2} = -\sigma_2 \frac{\partial \mathcal{Z}}{\partial \sigma_1} = 0.$$

The critical points (CP) of tangency are called of the ‘first kind’ (CP1), according to the terminology introduced in [7], and they represent periodic orbits under the complete 2-DOF flow of the Hamiltonian (23) (see subsection 3.1). We distinguish two subcases (see Fig. 4):

Inner tangency: in a neighborhood enclosing the point of tangency, the curve $\mathcal{C}_{\sigma_0, \mathcal{E}^{(P_1)}}^{(\sigma_2=0)}$ is contained within the disc limited by the circle $\mathcal{S}_{\sigma_0}^{(\sigma_2=0)}$ (point P_1 in Fig. 4). Then, in the same neighborhood the constant energy surface $\mathcal{C}_{\sigma_0, \mathcal{E}^{(P_1)}}$ intersects the sphere \mathcal{S}_{σ_0} at two closed loops joining each other at the singular point P_1 . The fixed point P_1 corresponds to a Floquet-unstable periodic orbit, and the

two loops to the separatrices asymptotically connected to the periodic orbit.

Outer tangency: in a neighborhood enclosing the point of tangency, the curve $\mathcal{C}_{\sigma_0, \mathcal{E}^{(P_2)}}^{(\sigma_2=0)}$ is not contained within the disc limited by the circle $\mathcal{S}_{\sigma_0}^{(\sigma_2=0)}$ (point P_2 in Fig. 4). Then, the constant energy surface $\mathcal{C}_{\sigma_0, \mathcal{E}^{(P_2)}}$ has no common points with the sphere \mathcal{S}_{σ_0} in the same neighborhood other than P_2 . The fixed point corresponds to a Floquet-stable periodic orbit. For values of the energy $\mathcal{E} \approx \mathcal{E}^{(P_2)}$ we obtain surfaces $\mathcal{C}_{\sigma_0, \mathcal{E}}$ which intersect the sphere at closed curves near to, and surrounding P_2 . These are invariant curves of the reduced flow representing 2-tori of the complete flow around the stable periodic orbit.

3.3.2 Case II: degenerate transverse intersection of \mathcal{S}_{σ_0} with $\mathcal{C}_{\sigma_0, \mathcal{E}}$

At those points $(\sigma_{1,F}, \sigma_{3,F})$ where

$$\left(\frac{\partial \mathcal{Z}}{\partial \sigma_1} \right)_{\sigma_1=\sigma_{1,F}, \sigma_3=\sigma_{3,F}; \sigma_0} = \left(\frac{\partial \mathcal{Z}}{\partial \sigma_3} \right)_{\sigma_1=\sigma_{1,F}, \sigma_3=\sigma_{3,F}; \sigma_0} = 0 \quad (33)$$

(that is, Eq. (31) with $\mu = 0$) the surface $\mathcal{C}_{\sigma_0, \mathcal{E}^{(F)}}$, with $\mathcal{E}^{(F)} = \mathcal{Z}(\sigma_{1,F}, \sigma_{3,F}; \sigma_0)$ reduces either to a single straight line parallel to the σ_2 -axis, or to two sheets intersecting along a line parallel to the σ_2 -axis. If the line intersects transversally the sphere \mathcal{S}_{σ_0} (see Fig. 5) we obtain two fixed points of the flow F_1, F_2 on the sphere, i.e. two periodic orbits of the complete flow. Such critical points (or orbits) are called of the ‘second kind’ (CP2). Their stability depends on the sign-definiteness of the quadratic form $(\partial^2 \mathcal{Z} / \partial \sigma_1^2) \delta \sigma_1^2 + 2(\partial^2 \mathcal{Z} / \partial \sigma_1 \partial \sigma_3) \delta \sigma_1 \delta \sigma_3 + (\partial^2 \mathcal{Z} / \partial \sigma_3^2) \delta \sigma_3^2$ where the partial derivatives are evaluated at $\sigma_1 = \sigma_{1,F}$, $\sigma_3 = \sigma_{3,F}$. If the quadratic form is sign-definite, the points F_1, F_2 are linearly stable. For values of the energy \mathcal{E} near $\mathcal{E}^{(F)}$ the surface $\mathcal{C}_{\sigma_0, \mathcal{E}}$ has the form of a cylinder with elliptic cross-section which surrounds the axis $\mathcal{C}_{\sigma_0, \mathcal{E}^{(F)}}$, and its intersections with the sphere are elliptic-like curves which surround the fixed points F_1 or F_2 and represent 2-tori of the complete flow around the periodic orbits corresponding to the points F_1 or F_2 (see top row in Fig. 5). In the case, however, where the sign of the quadratic form is indefinite, the points F_1, F_2 represent unstable periodic orbits, and the surface $\mathcal{C}_{\sigma_0, \mathcal{E}^{(F)}}$, together with nearby surfaces for energies close to $\mathcal{E}^{(F)}$ intersect the sphere forming saddles around each of the points F_1 or F_2 (bottom row in Fig. 5).

3.4 Analytical formulas

In the present section we implement our geometric method to analyze the sequence of bifurcations produced in the case in which the planetary system has a small AMD value, i.e. the planetary orbits (2D or 3D) never become very inclined and very eccentric. This allows to adopt a low-order truncation model for the secular Hamiltonian, written generically in Hopf variables as

$$\mathcal{K}_I(\sigma_1, \sigma_3; \sigma_0) = A\sigma_1^2 + C\sigma_3^2 + B\sigma_1\sigma_3 + (D_1\sigma_0 + \tilde{\Delta}_1)\sigma_1 + (D_3\sigma_0 + \tilde{\Delta}_3)\sigma_3 . \quad (34)$$

Without loss of generality, through a rotation we can set $B = 0$, hence getting the following generic Hamiltonian

$$\mathcal{K}_I(\sigma_1, \sigma_3; \sigma_0) = \mathcal{A}\sigma_1^2 + \mathcal{C}\sigma_3^2 + (\mathcal{D}_1\sigma_0 + \Delta_1)\sigma_1 + (\mathcal{D}_3\sigma_0 + \Delta_3)\sigma_3 \quad (35)$$

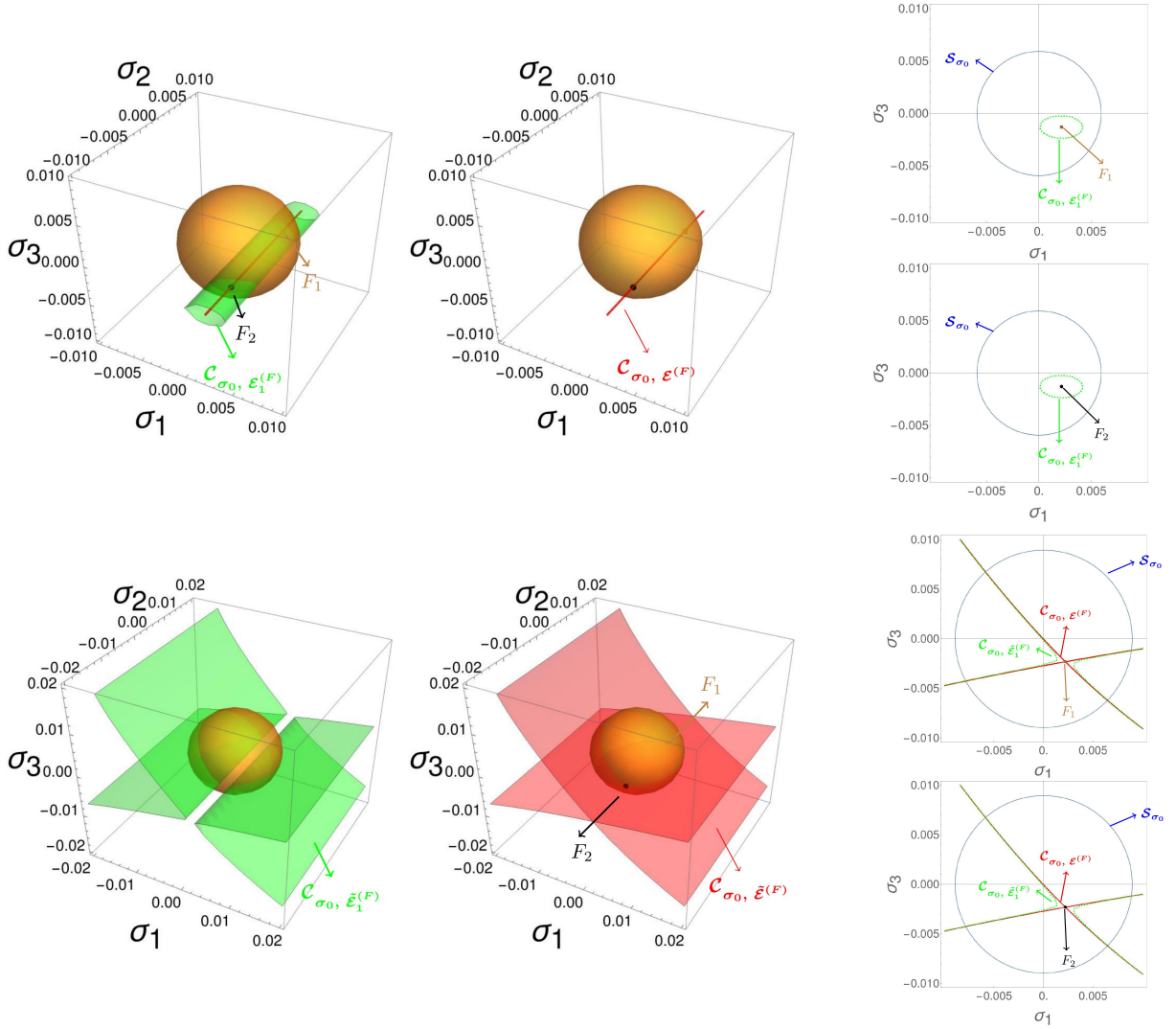


Figure 5: Graphical representation of the critical points of second kind F_1 and F_2 . Top: elliptic case (see text). The example is taken from the choice of integrable model $\mathcal{Z} = \mathcal{H}_{int}$, and it corresponds to the phase portrait $\mathcal{P}_{\mathcal{Z}}(\sigma_0)$ with $\sigma_0 = 5.93 \cdot 10^{-3}$ (the third panel in the top row of Fig. 6). Bottom: hyperbolic case. The example is taken from the choice of integrable model $\mathcal{Z} = \mathcal{H}_{int}^{(1)}$, and it corresponds to the phase portrait $\mathcal{P}_{\mathcal{Z}}(\sigma_0)$ with $\sigma_0 = 8.94 \cdot 10^{-3}$ (see Fig. 8). In both cases, the left panel shows the intersection of the sphere \mathcal{S}_{σ_0} with an energy surface $\mathcal{C}_{\sigma_0, \epsilon}$ for $\mathcal{E} \approx \mathcal{E}^{(F)}$ and $\mathcal{E} \approx \tilde{\mathcal{E}}^{(F)}$, the middle panel for $\mathcal{E} = \mathcal{E}^{(F)}$ and $\mathcal{E} = \tilde{\mathcal{E}}^{(F)}$, and the right panels the corresponding projections to the plane $\sigma_2 = 0$ (intersection of the curves $\mathcal{C}_{\sigma_0, \epsilon}^{(\sigma_2=0)}$ with the circles $\mathcal{S}_{\sigma_0}^{(\sigma_2=0)}$). We have $\mathcal{E} = \mathcal{E}_1^{(F)} = -1.7362 \cdot 10^{-5}$ and $\mathcal{E}^{(F)} = -1.7366 \cdot 10^{-5}$ in the top row, in which the corresponding surfaces are a cylinder (left panel) reducing to a straight line (middle panel). We have $\mathcal{E} = \tilde{\mathcal{E}}_1^{(F)} = -2.874 \cdot 10^{-5}$ and $\tilde{\mathcal{E}}^{(F)} = -2.87453 \cdot 10^{-5}$ in the bottom panel, where the corresponding surfaces are hyperbolic sheets (left panel) reducing to two sheets intersecting at the line $F_1 F_2$ in the middle panel.

with \mathcal{A} , \mathcal{C} , \mathcal{D}_1 , \mathcal{D}_3 , Δ_1 , Δ_3 control parameters. The rotation leading to $B = 0$ is a linear change of coordinates $(\sigma_0, \sigma_1, \sigma_2, \sigma_3) \rightarrow (\tilde{\sigma}_0, \tilde{\sigma}_1, \tilde{\sigma}_2, \tilde{\sigma}_3)$ such that $\sigma_0 = \tilde{\sigma}_0$, $\sigma_2 = \tilde{\sigma}_2$ and

$$\sigma_1 = \alpha \tilde{\sigma}_1 + \beta \tilde{\sigma}_3, \quad \sigma_3 = -\beta \tilde{\sigma}_1 + \alpha \tilde{\sigma}_3 \quad (36)$$

for some sine and cosine coefficients α and β computed so that

$$\alpha^2 + \beta^2 = 1 \quad \text{and} \quad B\alpha^2 + 2A\alpha\beta - 2C\alpha\beta - B\beta^2 = 0 .$$

Resulting from a rotation, the coordinates $(\tilde{\sigma}_0, \tilde{\sigma}_1, \tilde{\sigma}_2, \tilde{\sigma}_3)$ still satisfy the condition of sphere (27) as well as the Poisson algebra $\{\tilde{\sigma}_i, \tilde{\sigma}_j\} = -2\epsilon_{ijk}\tilde{\sigma}_k$, $i, j, k = 1, 2, 3$. Moreover $\sigma_0 = \tilde{\sigma}_0$ is also a Casimir invariant of the algebra in the new variables. Hence, computing the values of $\tilde{\sigma}_0$ for which the CP occurs (i.e, solving Eqs. (40) and (41)) is equivalent to finding the radius σ_0 for which the sphere and the surface $\mathcal{C} = \mathcal{E}$ are tangent. For the sake of simplicity, in the following examples we perform the rotation (36) whenever needed and then simply rename the variables $(\tilde{\sigma}_0, \tilde{\sigma}_1, \tilde{\sigma}_2, \tilde{\sigma}_3)$ in Eq. (35) as $(\sigma_0, \sigma_1, \sigma_2, \sigma_3)$.

The advantage on considering a low-order system is that implementing the geometric method of the previous sections leads to analytical formulas allowing to predict the form and sequence of the bifurcations of periodic orbits stemming from the basic ACR states.

To find the non-degenerate critical points of the type CP1 of the Hamiltonian (35) we solve Eq.(31), with the assumption that $(\mathcal{D}_1\sigma_0 + \Delta_1)$ and $(\mathcal{D}_3\sigma_0 + \Delta_3)$ are not both vanishing. This gives

$$\begin{aligned} \sigma_1^{(CP1)}(\mu, \sigma_0) &= -\frac{\mathcal{D}_1\sigma_0 + \Delta_1}{2(\mathcal{A} - \mu)} , \\ \sigma_2^{(CP1)}(\mu, \sigma_0) &= 0 , \\ \sigma_3^{(CP1)}(\mu, \sigma_0) &= -\frac{\mathcal{D}_3\sigma_0 + \Delta_3}{2(\mathcal{C} - \mu)} . \end{aligned} \quad (37)$$

Implementing the constraint

$$\mathcal{S}(\mu, \sigma_0) = (\sigma_1^{(CP1)}(\mu, \sigma_0))^2 + (\sigma_3^{(CP1)}(\mu, \sigma_0))^2 - \sigma_0^2 = 0 ,$$

we can look for the conditions to have more than two solutions (in μ) as an effect of changing σ_0 [7]. The numerator of $\mathcal{S}(\mu, \sigma_0) = 0$ corresponds to an equation of 4th degree in μ , namely

$$4(\mathcal{A} - \mu)^2(\mathcal{C} - \mu)^2 - (\mathcal{A} - \mu)^2 \mathcal{T}_3(\sigma_0) - (\mathcal{C} - \mu)^2 \mathcal{T}_1(\sigma_0) = 0 , \quad (38)$$

where

$$\mathcal{T}_1(\sigma_0) = \left(\mathcal{D}_1 + \frac{\Delta_1}{\sigma_0} \right)^2 , \quad \mathcal{T}_3(\sigma_0) = \left(\mathcal{D}_3 + \frac{\Delta_3}{\sigma_0} \right)^2 .$$

When the number of real solutions of the above equation changes, we have the corresponding *bifurcation value* of σ_0 . The discriminant of (38) w.r.t. μ is a function in σ_0 whose simple zeros provide the required change in the number of solutions. It is given by

$$\begin{aligned} \mathcal{Q}(\sigma_0) &= 64(\mathcal{A} - \mathcal{C})^2 \mathcal{T}_1(\sigma_0) \mathcal{T}_3(\sigma_0) \left[(4(\mathcal{A} - \mathcal{C})^2 - \mathcal{T}_1(\sigma_0))^3 - 3\mathcal{T}_3(\sigma_0) \left(16(\mathcal{A} - \mathcal{C})^4 \right. \right. \\ &\quad \left. \left. + 28\mathcal{T}_1(\sigma_0)(\mathcal{A} - \mathcal{C})^2 + \mathcal{T}_1(\sigma_0)^2 \right) + 3\mathcal{T}_3(\sigma_0)^2 (4(\mathcal{A} - \mathcal{C})^2 - \mathcal{T}_1(\sigma_0)) - \mathcal{T}_3(\sigma_0)^3 \right] \end{aligned} \quad (39)$$

Notice that $\mathcal{T}_1(\sigma_0) = 0$ or $\mathcal{T}_3(\sigma_0) = 0$ do not correspond to a change in the sign of the discriminant. At $\mathcal{A} = \mathcal{C}$ the discriminant is identically zero for every value of σ_0 ; this is the situation at which the ellipses degenerate to circles. Therefore, tangencies with the phase space can occur either at an infinite number of points or at no point. Higher order normal forms would be needed to describe the bifurcations. We do not consider this case here. By solving $\mathcal{Q}(\sigma_0) = 0$ with respect to $\mathcal{T}_3(\sigma_0)$ and considering the only real solution, the bifurcation values of σ_0 can be found by imposing

$$f_1(\sigma_0) = 0$$

where

$$f_1(\sigma_0) = -4(\mathcal{A}-\mathcal{C})^2 + \mathcal{T}_1(\sigma_0) + \mathcal{T}_3(\sigma_0) - 2^{2/3} 3 \left((\mathcal{A}-\mathcal{C})^2 \mathcal{T}_1(\sigma_0)^2 \right)^{1/3} + 2^{1/3} 6 \left((\mathcal{A}-\mathcal{C})^4 \mathcal{T}_1(\sigma_0) \right)^{1/3}. \quad (40)$$

Instead, the bifurcation values of σ_0 for fixed points of the type CP2 can be found by solving

$$f_2(\sigma_0) = -4 + \frac{\mathcal{T}_1(\sigma_0)}{\mathcal{A}^2} + \frac{\mathcal{T}_3(\sigma_0)}{\mathcal{C}^2} = 0.$$

The solution in this case can be explicitly found:

$$\begin{aligned} \sigma_0^{(CP2,1)} &= -\frac{\mathcal{C}^2 \mathcal{D}_1 \Delta_1 + \mathcal{A}^2 \mathcal{D}_3 \Delta_3 + \mathcal{A} \mathcal{C} \sqrt{4\mathcal{C}^2 \Delta_1^2 - (\mathcal{D}_3 \Delta_1 + 2\mathcal{A} \Delta_3 - \mathcal{D}_1 \Delta_3)(\mathcal{D}_3 \Delta_1 - (2\mathcal{A} + \mathcal{D}_1) \Delta_3)}}{\mathcal{C}^2 \mathcal{D}_1^2 + \mathcal{A}^2 (-4\mathcal{C}^2 + \mathcal{D}_3^2)}, \\ \sigma_0^{(CP2,2)} &= -\frac{\mathcal{C}^2 \mathcal{D}_1 \Delta_1 + \mathcal{A}^2 \mathcal{D}_3 \Delta_3 - \mathcal{A} \mathcal{C} \sqrt{4\mathcal{C}^2 \Delta_1^2 - (\mathcal{D}_3 \Delta_1 + 2\mathcal{A} \Delta_3 - \mathcal{D}_1 \Delta_3)(\mathcal{D}_3 \Delta_1 - (2\mathcal{A} + \mathcal{D}_1) \Delta_3)}}{\mathcal{C}^2 \mathcal{D}_1^2 + \mathcal{A}^2 (-4\mathcal{C}^2 + \mathcal{D}_3^2)}. \end{aligned} \quad (41)$$

Geometrically, the appearance of the CP2 is due to the centers of the ellipses or hyperbolas entering or leaving the circle $\mathcal{S}_{\sigma_0}^{(\sigma_2=0)} : \sigma_1^2 + \sigma_3^2 = \sigma_0^2$.

4 Application to different integrable models approximating the secular Hamiltonian

4.1 Integrable Hamiltonian \mathcal{H}_{int}

As a first example of application of the geometric method exposed to Section 3, we consider the integrable Hamiltonian \mathcal{H}_{int} (Eq. (5)). Up to terms of second order in the variables σ_i (i.e. of fourth order in the eccentricities), apart from constants, we find the approximate formula

$$\mathcal{H}_{int} \approx A\sigma_1^2 + C\sigma_3^2 + B\sigma_1\sigma_3 + D(\sigma_0)\sigma_1 + E(\sigma_0)\sigma_3 + F(\sigma_0)$$

where, for the parameters (masses, semi-major axes, and AMD value) as in the ν -Andromedæ system (see [13]) the coefficients read:

$$\begin{aligned} A &= 0.00212824, & C &= 0.00186469, \\ B &= -0.00186482, & D(\sigma_0) &= 0.000165361 - 0.0159745 \sigma_0, \\ E(\sigma_0) &= 0.0000214817 - 0.00532338 \sigma_0, & F(\sigma_0) &= -0.00214065 \sigma_0 - 0.108446 \sigma_0^2. \end{aligned}$$

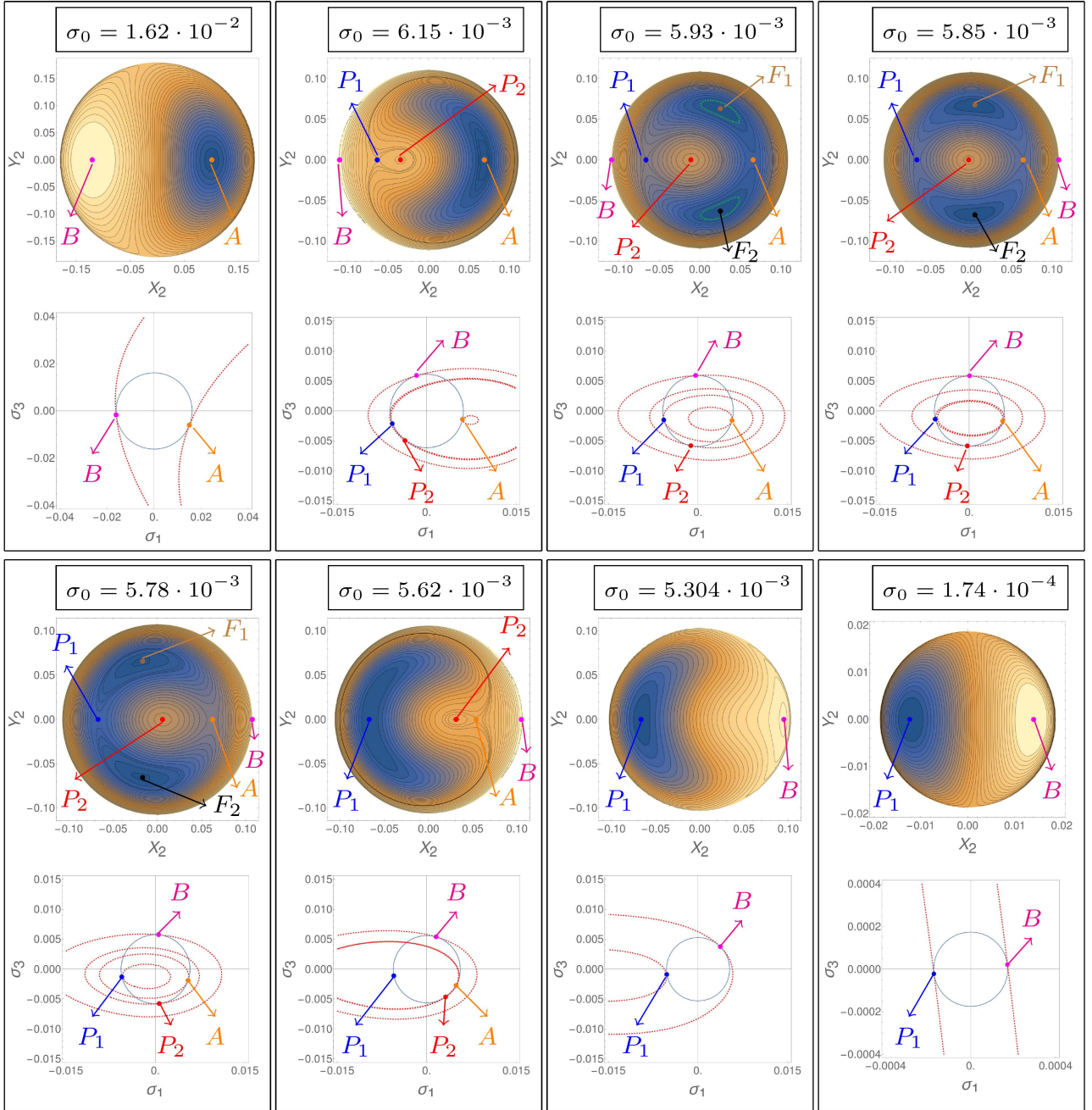


Figure 6: The first and third rows show the contour plots $\mathcal{P}_{\mathcal{H}_{int}}(\sigma_0; \text{AMD})$ (same as in Fig. 2), where the position of the fixed points (indicated by colored points) has been computed by the tangency method (see text). The second and fourth rows show the intersections of the spheres \mathcal{S}_{σ_0} (blue curve $\mathcal{S}_{\sigma_0}^{(\sigma_2=0)}$) with the energy surfaces $\mathcal{C}_{\sigma_0, \mathcal{E}}$ (red dashed curves $\mathcal{C}_{\sigma_0, \mathcal{E}}^{(\sigma_2=0)}$) with the plane (σ_1, σ_3) for $\sigma_2 = 0$, for different values of the energy \mathcal{E} and values of σ_0 as indicated in each panel.

The coefficients A, B, C satisfy $B^2 < 4AC$, hence the quadratic form $A\sigma_1^2 + C\sigma_3^2 + B\sigma_1\sigma_3$ yields ellipses. Thus, for any permissible value \mathcal{E} , the curve $\mathcal{C}_{\sigma_0, \mathcal{E}}^{(\sigma_2=0)}$ is ellipse-like.

Figure 6 shows the phase portraits $\mathcal{P}_{\mathcal{H}_{int}}(\sigma_0)$ in the above model. Altering the value of σ_0 as indicated in each panel, we obtain fixed points of both classes CP1 and CP2 in the phase portraits (first and third row). These are compared with the fixed points found through the curves $\mathcal{S}_{\sigma_0}^{(\sigma_2=0)}$ and $\mathcal{C}_{\sigma_0, \mathcal{E}}^{(\sigma_2=0)}$. As σ_0 decreases, implying a smaller value of the total angular momentum, the general level of mutual inclination of the orbits increases (from top left to bottom right in Fig. 6). The top left panel shows the starting point of the observed bifurcation sequence, where we have the two fixed points A and B corresponding to the basic ACR states. These are tangency points of \mathcal{S}_{σ_0} with $\mathcal{C}_{\sigma_0, \mathcal{E}}$ at the values $\sigma_0 = \sigma_{0,max} (= 1.62 \cdot 10^{-2})$ and the energies $\mathcal{E} = \mathcal{E}_{min}$ for the mode A, and $\mathcal{E} = \mathcal{E}_{2,3}$ for the mode B (cf. with caption in Fig. 3). Both A and B are points of outer tangency of the curves $\mathcal{S}_{\sigma_0}^{(\sigma_2=0)}$ and $\mathcal{C}_{\sigma_0, \mathcal{E}}^{(\sigma_2=0)}$, hence linearly stable. It is easy to verify that $\psi^{(A)} = 0$ and $\psi^{(B)} = \pi$, leading to $\varpi_3 = \varpi_2 + \pi$ (perihelia anti-aligned) and $\varpi_3 = \varpi_2$ (perihelia aligned). Hence, the associated orbits yield two coplanar ellipses with, respectively, anti-aligned and aligned pericenters precessing with the same frequency.

Decreasing the value of σ_0 , at the second frame on the top of Fig. 6, a *saddle-node* bifurcation takes place, giving rise to two new fixed points, i.e., the periodic orbits P_1 and P_2 . P_1 corresponds to an inner tangency of the curves $\mathcal{S}_{\sigma_0}^{(\sigma_2=0)}$ with $\mathcal{C}_{\sigma_0, \mathcal{E}}^{(\sigma_2=0)}$ (unstable), while P_2 corresponds to an outer tangency (stable) (see Fig. 4). Besides these orbits, we still have present in the phase portraits the stable fixed points A and B (outer tangencies) of the ACR states. However, the ellipse yielding the outer tangency of the fixed point A gradually shrinks in size as σ_0 decreases. Then, at a critical value of $\sigma_0 = \sigma_0^{(A)}$ the ellipse shrinks to a point, while, for still lower values, as in the third top panel of Fig. 6, the tangent ellipse re-emerges, being now contained in the disc limited by $\mathcal{S}_{\sigma_0}^{(\sigma_2=0)}$, yielding now a fixed point A of inner tangency, hence unstable. At the critical value $\sigma_0^{(A)}$ we then have a pitchfork bifurcation, accompanied with the birth of two new stable fixed points (F_1 and F_2), not shown in the second and fourth rows of Fig. 6 since they are of the type CP2, i.e., out of the plane $\sigma_2 = 0$. For values of σ_0 smaller than $\sigma_0^{(A)}$, there are surfaces $\mathcal{C}_{\sigma_0, \mathcal{E}}$ of the form of the elliptic cylinders, as in the left panel of Fig. 5, which intersect transversely with the sphere \mathcal{S}_{σ_0} . The intersection yield invariant curves forming the islands of stability around the fixed points F_1 and F_2 . The latter correspond to the value of the energy $\mathcal{E}^{(F)}$ at which the elliptic cylinders collide to straight lines (middle panel in Fig. 5). In the third, fourth and fifth panel we find elliptic cylinders for energies $\mathcal{E} > \mathcal{E}^{(F)}$. However, decreasing further σ_0 , the fixed points F_1, F_2 eventually collide with P_1 (sixth panel in Fig. 6), and this collision terminates the F -family of periodic orbits by an inverse pitchfork bifurcation which renders the point P_1 stable. Note that this process is equivalent to the one of the birth of the F -family, since, at the point of the collision the tangency corresponding to the point P_1 turns from inner to outer, i.e., the point P_1 turns from unstable to stable. Finally, decreasing σ_0 still further, the points P_2 and A similarly disappear by an inverse saddle-node bifurcation. Hence, the only surviving periodic orbits for small σ_0 are the stable orbits P_1 and B.

As regards its comparison with the full Hamiltonian, simple visual comparison between Figs. 6 and 1 shows that the model \mathcal{H}_{int} does not capture the correct sequence of bifurcations of periodic orbits seen in the phase portraits obtained by the full 3D secular Hamiltonian model \mathcal{H}_{sec} . This is remedied, however, computing a higher order secular normal form, as discussed in the next subsection.

4.2 Secular normal form $\mathcal{H}_{int}^{(1)}$

A second integrable model, giving rise to a better integrable approximation of the Hamiltonian model \mathcal{H}_{sec} , can be derived by constructing a *secular normal form* of the Hamiltonian \mathcal{H}_{sec} . As shown below, a first order normal form leads to an integrable model able to qualitatively recover the correct sequence of bifurcations found in the full model \mathcal{H}_{sec} .

To compute the normal form, we make use of the ‘book-keeping method’ discussed in [4]. Starting from the Hamiltonian of Eq. (13) written in the canonical variables of Eq. (22)

$$\mathcal{H}_{sec}(\psi, \varphi, \Gamma, J) = \mathcal{H}_{int}(\psi, \Gamma; J) + \mathcal{H}_{1,space}(\psi, \varphi, \Gamma, J)$$

\mathcal{H}_{int} is decomposed as

$$\mathcal{H}_{int}(\psi, \Gamma; J) = Z_0(J) + \lambda Z_{0,1}(\psi, \Gamma; J).$$

where

$$Z_0(J) = c + \omega J \tag{42}$$

is the normal form term (with c a constant value) and λ is a ‘book-keeping’ symbol, numerically equal to $\lambda = 1$, used to organize all the normal form series terms in groups of similar order of smallness. Using the ‘book-keeping’ notation, we rewrite the Hamiltonian as

$$\mathcal{H}^{(0)} = \mathcal{H}_{sec}(\psi, \varphi, \Gamma, J) = Z_0(J) + \lambda Z_{0,1}(\psi, \Gamma; J) + \lambda \mathcal{H}_{1,space}(\psi, \varphi, \Gamma, J). \tag{43}$$

All the terms contained in $\mathcal{H}_{1,space}$ depend on the angle φ . We then define the Lie generating function χ as the solution of the following homological equation:

$$\{Z_0, \chi\} + \lambda \mathcal{H}_{1,space} = 0. \tag{44}$$

To solve the homological equation, we first re-express the Hamiltonian in the variables (w_2, w_3, W_2, W_3) , introduced in Eq. (11), rather than $(\psi, \varphi, \Gamma, J)$. Then

$$\mathcal{H}_{sec}(w_2, w_3, W_2, W_3) = \mathcal{H}_{int}(w_2 - w_3, W_2, W_3) + \mathcal{H}_{1,space}(w_2, w_3, W_2, W_3)$$

where

$$\mathcal{H}_{int} = Z_0(W_2, W_3) + \lambda Z_{0,1}(w_2 - w_3, W_2, W_3),$$

with

$$Z_0(W_2, W_3) = c + aW_2 + bW_3. \tag{45}$$

We then obtain

$$\mathcal{H}^{(0)} = \mathcal{H}_{sec}(w_2, w_3, W_2, W_3) = Z_0(W_2, W_3) + \lambda Z_{0,1}(w_2 - w_3, W_2, W_3) + \lambda \mathcal{H}_{1,space}(w_2, w_3, W_2, W_3), \tag{46}$$

where $\mathcal{H}_{1,space}(w_2, w_3, W_2, W_3)$ contains trigonometric terms depending on linear combinations of the angles $k_1 w_2 + k_2 w_3$ with $k_1 + k_2 \neq 0$. Thus, writing the Taylor-Fourier expansion of $\mathcal{H}_{1,space}$ as

$$\mathcal{H}_{1,space}(\psi, \varphi, W_2, W_3) = \sum_{l,m,n,k} \theta_{l,m,n,k} W_2^l W_3^m e^{in\psi} e^{ik\varphi} = \sum_{l,m,n,k} \theta_{l,m,n,k} W_2^l W_3^m e^{i((n+k)w_2 - (n-k)w_3)}$$

the solution of the homological equation (44) reads

$$\chi(\psi, \varphi, W_2, W_3) = \lambda \sum_{\substack{l,m,n,k \\ k \neq 0 \wedge \\ a(n+k) \neq b(n-k)}} \frac{\theta_{l,m,n,k}}{i(a(n+k) - b(n-k))} W_2^l W_3^m e^{im\psi} e^{ik\varphi}.$$

Using χ , the one-step normalized Hamiltonian is given by

$$\mathcal{H}^{(1)} = \exp L_\chi \mathcal{H}^{(0)}, \quad (47)$$

where $\exp L_\chi \cdot = \sum_{j \geq 0} (L_\chi^j \cdot) / j!$ is the Lie series operator, $L_\chi \cdot = \{\cdot, \chi\}$ is the Lie derivative with respect to the dynamical function χ and $\{\cdot, \cdot\}$ denotes the Poisson bracket. Expanding Eq. (47) in powers of the book-keeping symbol λ , we find

$$\begin{aligned} \mathcal{H}^{(1)} &= \underbrace{Z_0 + \overbrace{\lambda Z_{0,1}}^{\mathcal{O}(\lambda)}}_{\mathcal{H}_{int}} + \underbrace{\lambda \mathcal{H}_{1,space} + \overbrace{\{Z_0, \chi\}}^{\mathcal{O}(\lambda)}}_{=0}} + \underbrace{\lambda \{Z_{0,1}, \chi\}}_{\mathcal{O}(\lambda^2)} + \underbrace{\lambda \{\mathcal{H}_{1,space}, \chi\}}_{\mathcal{O}(\lambda^2)} + \frac{1}{2} \underbrace{\{\{Z_0, \chi\}, \chi\}}_{\mathcal{O}(\lambda^2)} + \mathcal{O}(\lambda^3) \\ &= \mathcal{H}_{int} + \left\langle \frac{\lambda}{2} \{\mathcal{H}_{1,space}, \chi\} \right\rangle_\varphi + \mathcal{H}_{rest}^{(1)} + \mathcal{O}(\lambda^3), \end{aligned} \quad (48)$$

where

$$\mathcal{H}_{rest}^{(1)} = \lambda \{Z_{0,1}, \chi\} + \frac{\lambda}{2} \{\mathcal{H}_{1,space}, \chi\} - \left\langle \frac{\lambda}{2} \{\mathcal{H}_{1,space}, \chi\} \right\rangle_\varphi. \quad (49)$$

The average $\langle \cdot \rangle_\varphi$ means all terms independent of the angles or trigonometric terms depending only on the difference $\psi = w_2 - w_3$. Finally, we set

$$\mathcal{H}_{int}^{(1)} = \mathcal{H}_{int} + \left[\left\langle \frac{\lambda}{2} \{\mathcal{H}_{1,space}, \chi\} \right\rangle_\varphi \right]_{\leq N_{bk}}, \quad (50)$$

where the operation $[\cdot]_{N_{bk}}$ means to truncate the enclosed expression at the maximum adopted order of expansion in the eccentricities and inclinations ($N_{bk} = 12$ in our examples below). The integrable Hamiltonian model $\mathcal{H}_{int}^{(1)}$ is hereafter referred to as the first order *secular normal form* (or simply the ‘secular normal form’).

Phase portraits under the secular normal form $\mathcal{H}_{int}^{(1)}$ can be obtained using the change of variables (22) and (16) and computing Poincaré surfaces of section $\mathcal{PS}_{\mathcal{H}_{int}^{(1)}}(\mathcal{E}; \text{AMD})$ at a fixed level of energy \mathcal{E} through

$$\begin{aligned} \mathcal{PS}_{\mathcal{H}_{int}^{(1)}}(\mathcal{E}; \text{AMD}) &= \left\{ (X_2, Y_2, X_3, Y_3) \in \mathbb{R}^4 : \mathcal{H}_{int}^{(1)}(X_2, Y_2, X_3, Y_3 = 0; \text{AMD}) = \mathcal{E}, Y_3 = 0, \right. \\ &\quad \left. \dot{Y}_3 = -\frac{\partial \mathcal{H}_{int}^{(1)}}{\partial X_3} \Big|_{Y_3=0} \geq 0, \cos(i_{max}) \leq \cos(i_{mut})(X_2, Y_2, X_3, Y_3 = 0; \text{AMD}) \leq 1 \right\}. \end{aligned} \quad (51)$$

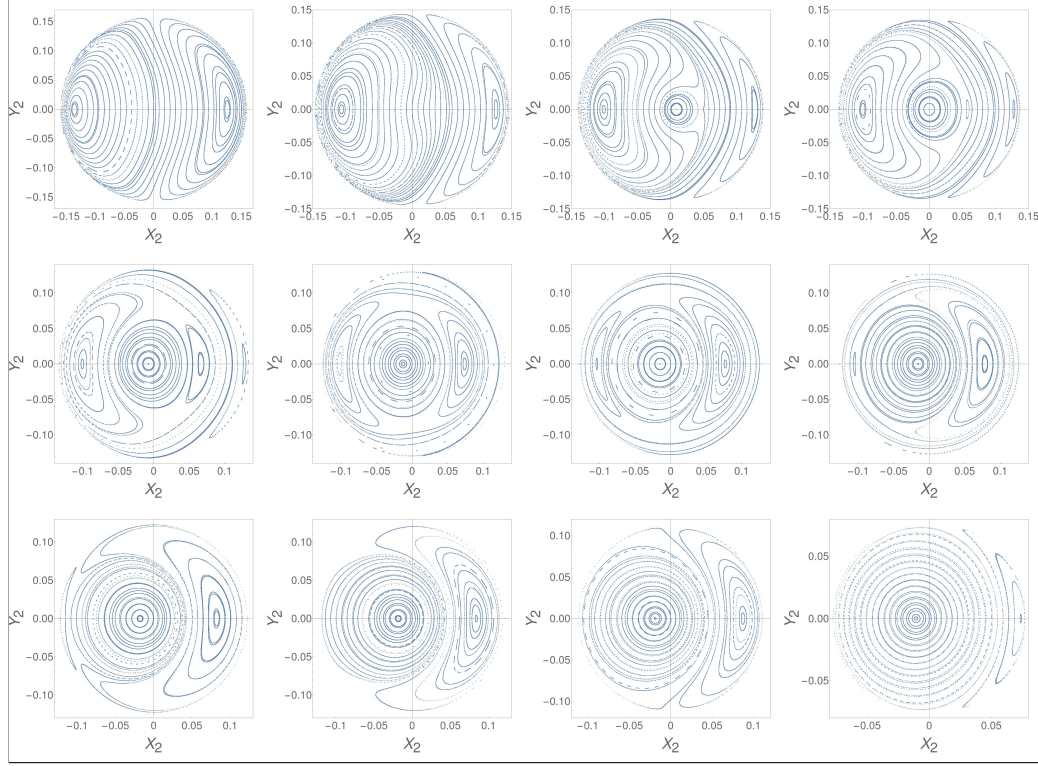


Figure 7: Poincaré surfaces of section $\mathcal{PS}_{\mathcal{H}_{int}^{(1)}}(\mathcal{E}; \text{AMD})$ in the plane (X_2, Y_2) with AMD fixed. The surfaces of section are computed by a numerical integration of trajectories of the normalized integrable Hamiltonian $\mathcal{H}_{int}^{(1)}$ (Eq. (50)) truncated at multipolar degree $N_P = 5$, order $N_{bk} = 12$ in the eccentricities, and energies (from top to bottom, from left to right) $\mathcal{E} = -5.82 \cdot 10^{-5}, -4.3 \cdot 10^{-5}, -3.59 \cdot 10^{-5}, -3.34 \cdot 10^{-5}, -3.03 \cdot 10^{-5}, -2.68 \cdot 10^{-5}, -2.51 \cdot 10^{-5}, -2.42 \cdot 10^{-5}, -2.12 \cdot 10^{-5}, -1.99 \cdot 10^{-5}, -1.44 \cdot 10^{-5}, -3.3 \cdot 10^{-6}$. In this case the energies for which we can have co-planar orbits range between $\mathcal{E}_{min} = -1.71 \cdot 10^{-4}$ and $\mathcal{E}_{2,3} = -5.82 \cdot 10^{-5}$. In the plot we consider the phase-portraits for energies $\mathcal{E} \geq \mathcal{E}_{2,3}$, for which no-coplanar orbits exist.

Figure 7 shows the surfaces of section for different (increasing, from left to right, from top to bottom) levels of energy. By visual inspection, the sequence of bifurcations produced by the secular normal form $\mathcal{H}_{int}^{(1)}$ differ considerably from those of the integrable hamiltonian \mathcal{H}_{int} before the normalization (top row of Fig. 2). The origin of the difference becomes clear by the analysis through Hopf variables as discussed below. On the other hand, comparison with the phase portraits of the full secular Hamiltonian \mathcal{H}_{sec} (Fig. 1) shows that the secular normal form reproduces qualitatively the same sequence of bifurcations as in the complete model, except for the last bifurcation (transition from the fourth to the fifth panel in Fig. 1), connected to the birth of the Lidov-Kozai periodic orbits. Such orbits are associated with the $e_2^2 \cos(2w_2)$ or $e_3^2 \cos(2w_3)$ terms in the secular Hamiltonian, which are not present in the secular normal form.

We now apply the geometric method of section 3 to the secular normal form $\mathcal{H}_{int}^{(1)}$ to recover the sequence of bifurcations observed in the regime of energies $\mathcal{E}_C \leq \mathcal{E} \leq \mathcal{E}_{C,2}$, where \mathcal{E}_C is the energy of the saddle-node bifurcation of the orbits P_1 and P_2 , and $\mathcal{E}_{C,2}$ is the energy of bifurcation of the Lidov-Kozai orbits. Similarly to Fig. 6, in the case of the secular normal form Fig. 8 yields the phase portraits of the secular normal form expressed in Hopf variables $\mathcal{H}_{int}^{(1)}(\sigma_1, \sigma_3; \sigma_0)$. Each upper panel in Fig. 8 corresponds to a fixed value of σ_0 decreasing from left to right and from top to bottom, and the invariant curves in the same portrait correspond to different values of the energy $\mathcal{E} = \mathcal{H}_{int}^{(1)}$ within the allowed limits computed in the same way as before for the Hamiltonian \mathcal{H}_{int} . The lower panel below each phase portrait shows the intersections or tangencies of various curves $\mathcal{C}_{\sigma_0, \mathcal{E}}^{(\sigma_2=0)}$ with the circle $\mathcal{S}_{\sigma_0}^{(\sigma_2=0)}$ for the corresponding value of σ_0 .

Comparing Figs. 6 and 8, we immediately notice that, for the same model parameters, the curves $\mathcal{S}_{\sigma_0}^{(\sigma_2=0)}$ are hyperbola-like in the case of the secular normal form, instead of ellipse-like, as in the Hamiltonian \mathcal{H}_{int} . Up to terms of second order in the variables σ_i , the secular normal form reads (apart from constants)

$$\mathcal{H}_{int}^{(1)} \approx A^{(1)}\sigma_1^2 + C^{(1)}\sigma_3^2 + B^{(1)}\sigma_1\sigma_3 + D^{(1)}(\sigma_0)\sigma_1 + E^{(1)}(\sigma_0)\sigma_3 + F^{(1)}(\sigma_0)$$

where, in our numerical example

$$\begin{aligned} A^{(1)} &= 0.00912208, & C^{(1)} &= -0.0518887, \\ B^{(1)} &= 0.00782589, & D^{(1)}(\sigma_0) &= 0.000425947 + 0.00634477 \sigma_0, \\ E^{(1)}(\sigma_0) &= 0.00101564 - 0.118017 \sigma_0, & F^{(1)}(\sigma_0) &= -0.0011129 \sigma_0 - 0.164326 \sigma_0^2. \end{aligned}$$

Hence, $(B^{(1)})^2 > 4A^{(1)}C^{(1)}$, implying that the quadratic form $A^{(1)}\sigma_1^2 + C^{(1)}\sigma_3^2 + B^{(1)}\sigma_1\sigma_3$ yields now a family of hyperbolas instead of ellipses. This difference brings essential differences in the structure of the phase portraits of the secular normal form $\mathcal{H}_{int}^{(1)}$ compared to the integrable model \mathcal{H}_{int} .

The sequence of bifurcations found in Fig. 8 can be summarized as follows: The top-left frame shows the starting phase portrait of the (near-)planar regime with the usual tangency points A and B associated with anti-aligned and aligned ACR orbits. Decreasing the value of σ_0 (second frame of Fig. 8, for $\sigma_0 = 1.023 \cdot 10^{-2}$) gives rise to a similar saddle-node bifurcation as in Fig. 6, with two new fixed points of the Poincaré map corresponding to periodic orbits P_1 and P_2 . However, due to the fact that the curves $\mathcal{C}_{\sigma_0, \mathcal{E}}^{(\sigma_2=0)}$ are now hyperbola-like, we note that the stability type of each of the orbits P_1 or P_2 is inverted with respect to Fig. 6. Thus, immediately after the bifurcation the tangent points belong to two nearby hyperbola-like curves, of which the curve containing the point P_1 yields an inner

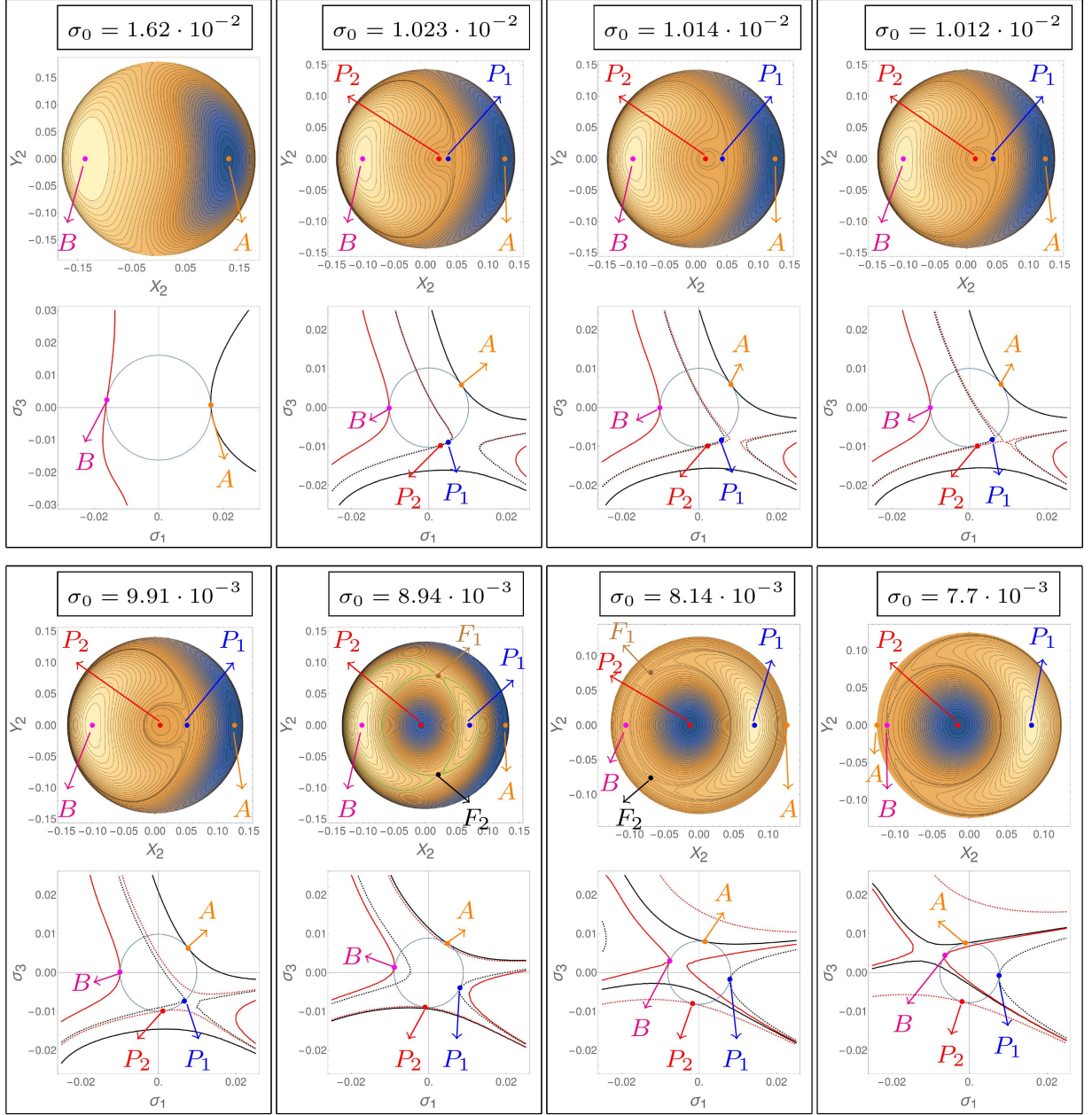


Figure 8: Upper panels: the contour plots $\mathcal{H}_{int}^{(1)}(X_2, Y_2; \sigma_0) = \mathcal{E}$, with $Y_3 = 0, \dot{Y}_3 \geq 0$ for decreasing values of σ_0 from top to bottom, left to right. Lower panels: intersections of and tangencies between the circles $\mathcal{S}_{\sigma_0}^{(\sigma_2=0)}$ (blue) and of the curves $\mathcal{C}_{\sigma_0, \mathcal{E}}^{(\sigma_2=0)}$ in the plane (σ_1, σ_3) , for different values of the energy \mathcal{E} and σ_0 fixed as in the upper frame corresponding to each lower frame. The points of tangency corresponding to CP1-type fixed points of the secular normal form are calculated by Eq. (32). The curves $\mathcal{C}_{\sigma_0, \mathcal{E}}^{(\sigma_2=0)}$ passing through the tangency points are hyperbola-like (compare with the corresponding curves in Fig. 6, which are ellipse-like).

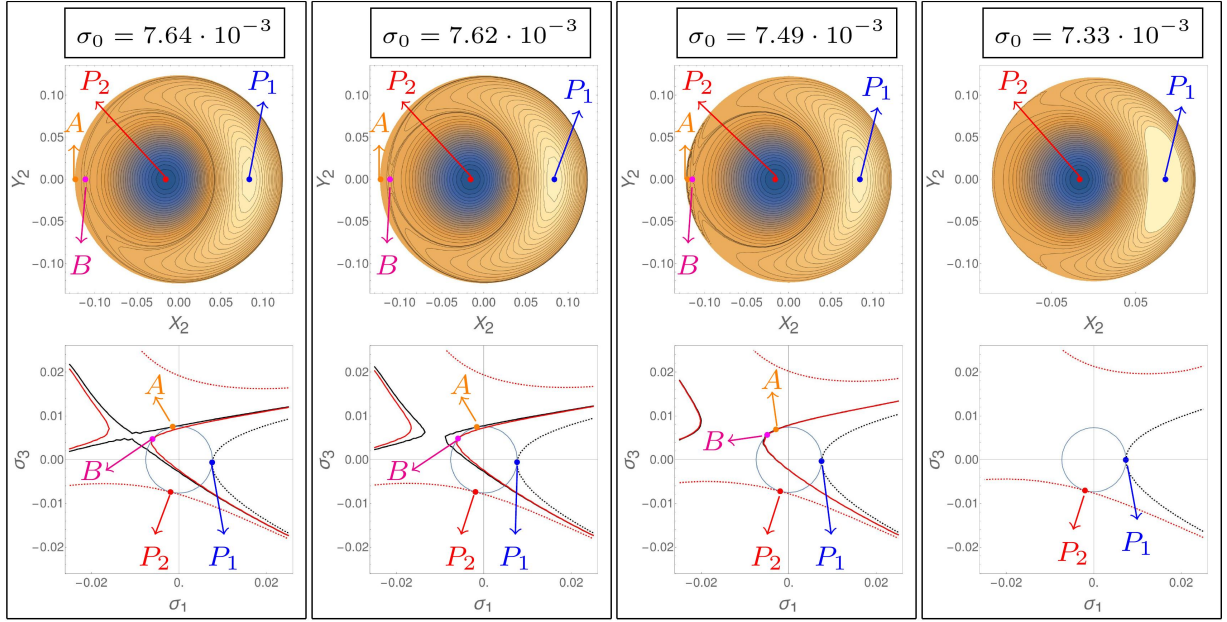


Figure 8: Continued.

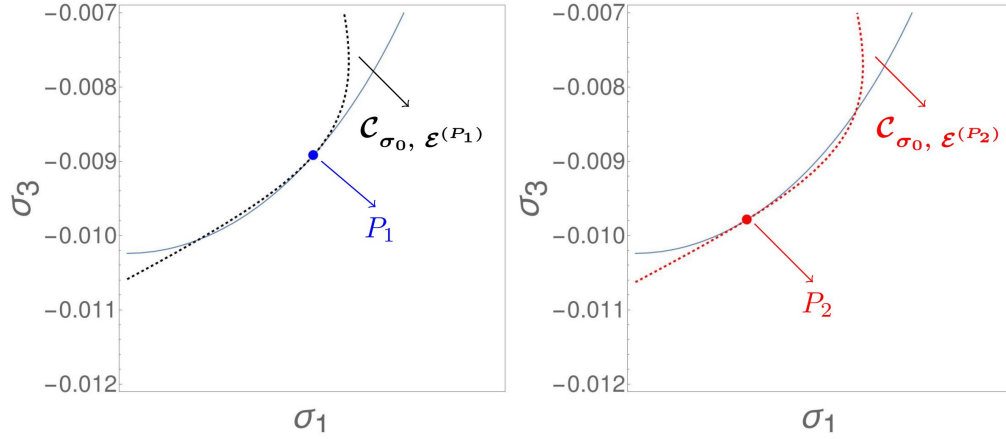


Figure 9: Zoom of the second plot of the second row of Fig. 8 (i.e. of the intersection between $\mathcal{S}_{\sigma_0}^{(\sigma_2=0)}$ and $\mathcal{C}_{\sigma_0, \mathcal{E}}^{(\sigma_2=0)}$ in the plane (σ_1, σ_3) for $\sigma_0 = 1.023 \cdot 10^{-2}$). The blue and red points are, respectively, unstable and stable since they are given by an inner and outer tangency between $\mathcal{S}_{\sigma_0}^{(\sigma_2=0)}$ and $\mathcal{C}_{\sigma_0, \mathcal{E}}^{(\sigma_2=0)}$. On the left we show the inner tangency between $\mathcal{S}_{\sigma_0}^{(\sigma_2=0)}$ and $\mathcal{C}_{\sigma_0, \mathcal{E}^{(P_1)}}^{(\sigma_2=0)}$ in P_1 , while on the right the outer tangency between $\mathcal{S}_{\sigma_0}^{(\sigma_2=0)}$ and $\mathcal{C}_{\sigma_0, \mathcal{E}^{(P_2)}}^{(\sigma_2=0)}$ in P_2 (in our example $\mathcal{E}^{(P_1)} = -3.78701$ and $\mathcal{E}^{(P_2)} = -3.78861$).

tangency (hence P_1 is unstable), while the curve containing the point P_2 yields an outer tangency

(hence P_2 is unstable) (see a zoom in Fig. 9). Decreasing further the value of σ_0 , we arrive at a critical value ($\sigma_0 \simeq 1.012 \cdot 10^{-2}$, see fourth panel in Fig. 8) where two independent hyperbola-like branches of the curve $\mathcal{C}_{\sigma_0, \mathcal{E}(P_2)}^{(\sigma_2=0)}$ join each other into a saddle point F . This point is outside the disc limited by the curve $\mathcal{S}_{\sigma_0}^{(\sigma_2=0)}$, hence it represents no possible new fixed point of the flows. Decreasing, however, σ_0 still further, the saddle point F moves towards the circle $\mathcal{S}_{\sigma_0}^{(\sigma_2=0)}$, and crosses it at a critical value of σ_0 which lies in the interval $8.94 \cdot 10^{-3} < \sigma_0 < 9.91 \cdot 10^{-3}$ (see the transition between the fifth and sixth panel of Fig. 8). At the crossing value we then have an inverse pitchfork bifurcation, whereby the point P_1 turns from unstable to stable, while for values of σ_0 below the critical one the saddle moves within the disc, giving rise to two unstable fixed points F_1 and F_2 of the CP2-type. For still smaller values of σ_0 , the saddle point F moves further inside the disc towards the left. Figure 10 gives the 3D picture of the intersection of the surfaces $\mathcal{C}_{\sigma_0, \mathcal{E}(F)}$ with the sphere \mathcal{S}_{σ_0} for $\sigma_0 = 8.94 \cdot 10^{-3}$ and for $\sigma_0 = 8.14 \cdot 10^{-3}$, corresponding to the sixth and seven panels in Fig. 8. Reducing σ_0 further, we then arrive at a second critical value lying in the interval $7.7 \cdot 10^{-3} < \sigma_0 < 8.14 \cdot 10^{-3}$ (see the transition between the seventh and eighth panel of Fig. 8), where the saddle point F crosses for a second time the circle $\mathcal{S}_{\sigma_0}^{(\sigma_2=0)}$, passing now from its interior to its exterior. At the second crossing we then have a second inverse pitchfork bifurcation turning the point B from stable to unstable. From this point on, decreasing σ_0 brings the saddle point F outside the disc, hence no longer yielding feasible fixed points of the system. In the same time, the ACR points B and A are given by an inner and outer tangency, hence they are unstable and stable respectively. Finally, reducing further σ_0 brings the separatrices of the fixed point B very close to the tangency point A. Hence, the area occupied by the island of stability around the fixed point A is necessarily reduced, while the areas of the domains of stability around the fixed points P_1 , and P_2 become large. As a consequence, the points P_1 and P_2 and their neighborhoods give now the dominant structures in the phase space (see 9th and 10th panel in Fig. 8), while the influence of the ACR orbits A, B is reduced. Then, at a third critical value of σ_0 in the interval $7.33 \cdot 10^{-3} < \sigma_0 < 7.49 \cdot 10^{-3}$ the points A, B, as well as the hyperbolas which contain them, collide. Then, the points A, B disappear altogether through an inverse saddle-node bifurcation (see the transition from the 11th to the 12th (last) panel in Fig. 8). From that point on, the only stable points surviving in the end of the sequence of bifurcations are P_1 and P_2 .

4.3 Secular normal form: octupole approximation $\tilde{\mathcal{H}}_{int}^{(N_P=3, N_{bk}=4)}$

Of all multipolar truncations of the secular Hamiltonian, the first non-integrable one is the *octupolar* approximation, corresponding to terms up to degree $N_P = 3$ in the semi-major axis ratio a_2/a_3 . In this case, assuming an expansion up to order $N_{bk} = 4$ in the eccentricities leads to the possibility of computing a secular normal form as in subsection 4.2, whose expression is an exact quadratic form in the Hopf variables as in Eq. (34). Explicit expressions for the normal form coefficients can be computed leading to:

$$\tilde{\mathcal{H}}_{int}^{(N_P=3, N_{bk}=4)} = A\sigma_1^2 + C\sigma_3^2 + B\sigma_1\sigma_3 + D(\sigma_0)\sigma_1 + E(\sigma_0)\sigma_3 + F(\sigma_0), \quad (52)$$

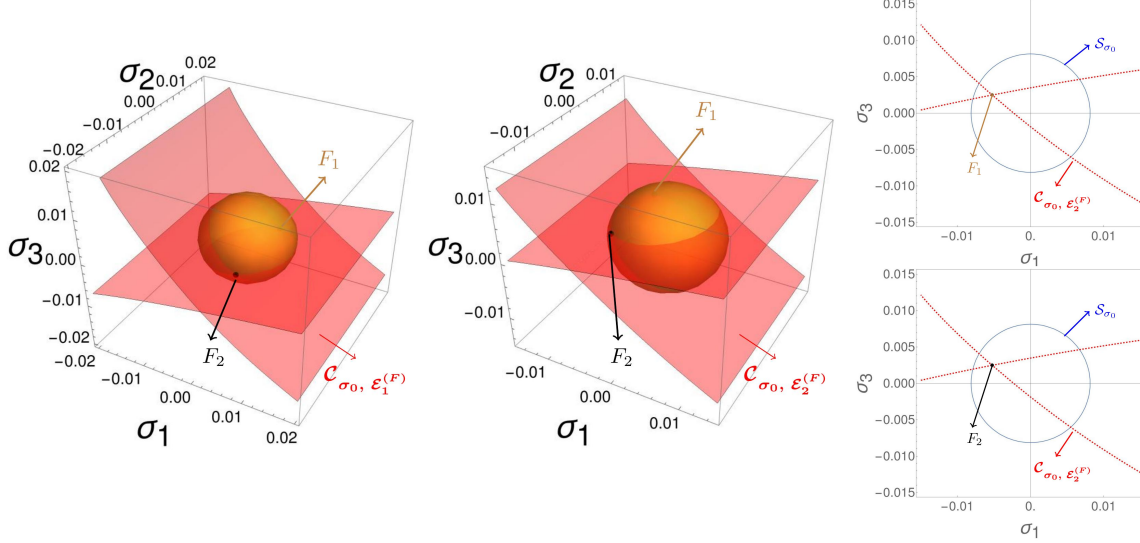


Figure 10: Graphical representation of the critical points of second kind F_1 and F_2 . Left: 3D representation of the sphere \mathcal{S}_{σ_0} and the surface $\mathcal{C}_{\sigma_0, \mathcal{E}_1^{(F)}}$, in the case $\sigma_0 = 8.94 \cdot 10^{-3}$, where $\mathcal{E}_1^{(F)}$ represents the energy of the fixed points F_1 and F_2 . We can observe that the surface of the energy pierces the sphere in the F -modes. Centre: As before, but in the case $\sigma_0 = 8.14 \cdot 10^{-3}$. For a value of the energy, namely $\mathcal{E}_2^{(F)}$, $\mathcal{C}_{\sigma_0, \mathcal{E}_2^{(F)}}$ pierces the sphere \mathcal{S}_{σ_0} in the points F_1 and F_2 of coordinates, respectively, $(\sigma_1^{(F)}, \sigma_2^{(F)}, \sigma_3^{(F)})$ and $(\sigma_1^{(F)}, -\sigma_2^{(F)}, \sigma_3^{(F)})$. Right: The projection of the 3D central plot (case $\sigma_0 = 8.14 \cdot 10^{-3}$) in the planes $\sigma_2 = 0$.

where the coefficients (apart from constants) are:

$$\begin{aligned}
A &= 0, \\
C &= -\frac{2025a_2^{9/2}\text{AMD}(\sqrt{a_2}m_2 + \sqrt{a_3}m_3)^2}{256a_3^{19/2}m_2m_3m_0^2(a+b)} + \frac{225a_2^2\text{AMD}}{64a_3^6m_0^2a} \left(\sqrt{\frac{a_2}{a_3}} \frac{m_3}{m_2} + \frac{a_2}{2a_3} + \frac{m_3^2}{2m_2^2} \right) \\
&\quad + \frac{3a_2}{8a_3^3m_0} \left(\frac{3}{2} \sqrt{\frac{a_2}{a_3}} - \frac{a_2m_2}{a_3m_3} + \frac{m_3}{4m_2} \right), \\
B &= \frac{675a_2^{13/4}\text{AMD}(\sqrt{a_2}m_2 + \sqrt{a_3}m_3)^2}{256a_3^{33/4}m_0^2m_2^{3/2}\sqrt{m_3}(a+b)} \left(\frac{b}{a} + 3 \right) + \frac{5a_2^{9/4}}{128a_3^{17/4}m_0} \left(57\sqrt{\frac{a_2m_2}{a_3m_3}} - 15\sqrt{\frac{m_3}{m_2}} \right), \\
D_1 &= \frac{2025a_2^{13/4}\text{AMD}(\sqrt{a_2}m_2 + \sqrt{a_3}m_3)^2}{256a_3^{33/4}m_0^2m_2^{3/2}\sqrt{m_3}(a+b)} \left(\frac{b}{a} + 3 \right) - \frac{105a_2^{9/4}}{128a_3^{17/4}m_0} \left(9\sqrt{\frac{a_2m_2}{a_3m_3}} + 7\sqrt{\frac{m_3}{m_2}} \right), \\
\Delta_1 &= -\frac{675a_2^{13/4}\text{AMD}^2(\sqrt{a_2}m_2 + \sqrt{a_3}m_3)^2}{256a_3^{33/4}m_0^2m_2^{3/2}\sqrt{m_3}(a+b)} \left(\frac{b}{a} + 3 \right) + \frac{165a_2^{9/4}\text{AMD}(\sqrt{a_2}m_2 + \sqrt{a_3}m_3)}{32a_3^{19/4}m_0\sqrt{m_2}\sqrt{m_3}} \\
&\quad - \frac{15a_2^{11/4}\sqrt{\mathcal{G}}\sqrt{m_2}\sqrt{m_3}}{16a_3^{17/4}\sqrt{m_0}}, \\
D_3 &= \frac{675a_2^2\text{AMD}}{32a_3^6m_0^2a} \left(\sqrt{\frac{a_2}{a_3}} \frac{m_3}{m_2} + \frac{a_2}{2a_3} + \frac{m_3^2}{2m_2^2} \right) + \frac{3a_2}{4a_3^3m_0} \left(\frac{3a_2m_2}{a_3m_3} - \frac{7m_3}{4m_2} \right), \\
\Delta_3 &= \frac{3a_2^{3/2}\sqrt{\mathcal{G}}}{8a_3^{7/2}\sqrt{m_0}} (\sqrt{a_2}m_2 - \sqrt{a_3}m_3) - \frac{225a_2^2\text{AMD}^2}{32a_3^6m_0^2a} \left(\sqrt{\frac{a_2}{a_3}} \frac{m_3}{m_2} + \frac{a_2}{2a_3} + \frac{m_3^2}{2m_2^2} \right) \\
&\quad + \frac{3a_2\text{AMD}}{2a_3^3m_0} \left(\frac{m_3}{m_2} - \frac{a_2m_2}{a_3m_3} \right).
\end{aligned}$$

The constants a and b correspond to secular frequencies (see Eq. (45)) and they are given by

$$a = -\frac{3\sqrt{\mathcal{G}}}{4a_3^{7/2}\sqrt{m_0}} \left(2a_2^{3/2}\sqrt{a_3}m_3 + a_2^2m_2 \right) + \frac{3a_2\text{AMD}}{4a_3^4m_0m_2m_3} \left(6\sqrt{a_2a_3}m_2m_3 + a_2m_2^2 + 5a_3m_3^2 \right),$$

$$b = -\frac{3\sqrt{\mathcal{G}}}{4a_3^{7/2}\sqrt{m_0}} \left(a_2^{3/2}\sqrt{a_3}m_3 + 2a_2^2m_2 \right) + \frac{3a_2\text{AMD}}{4a_3^4m_0m_2m_3} \left(6\sqrt{a_2a_3}m_2m_3 + 5a_2m_2^2 + a_3m_3^2 \right).$$

In our numerical example, dropping constants, as well as an irrelevant term depending only on σ_0 , the secular normal form in the octupole approximation resumes the form of Eq. (52) with

$$A = 0, \quad C = -0.0283636, \quad B = -0.029019,$$

$$D(\sigma_0) = 0.0011798 - 0.21118\sigma_0, \quad E(\sigma_0) = 0.00153399 - 0.270077\sigma_0.$$

After performing the preliminary rotation described in Subsection 4.2, it takes the form of Eq. (35):

$$\tilde{\mathcal{H}}_{int}^{(N_P=3, N_{bk}=4)} = \mathcal{K}_I(\tilde{\sigma}_1, \tilde{\sigma}_3; \sigma_0) = \mathcal{A}\tilde{\sigma}_1^2 + \mathcal{C}\tilde{\sigma}_3^2 + (\mathcal{D}_1\sigma_0 + \Delta_1)\tilde{\sigma}_1 + (\mathcal{D}_3\sigma_0 + \Delta_3)\tilde{\sigma}_3 \quad (53)$$

with

$$\mathcal{A} = 0.00610734, \quad \mathcal{C} = -0.0344709, \quad \mathcal{D}_1 = -0.089863,$$

$$\Delta_1 = 0.000492281, \quad \mathcal{D}_2 = -0.330852, \quad \Delta_2 = 0.00187156,$$

and Eqs. (40) and (41) can be solved explicitly yielding the bifurcation values in the parameter σ_0 where critical points of the first and second kind appear. We find $\sigma_0^{(CP1,1)} = 0.00489265$ and $\sigma_0^{(CP1,2)} = 0.00655611$, while the values $\sigma_0^{(CP2,1)} = 0.00623676$ and $\sigma_0^{(CP2,2)} = 0.00497142$ correspond to the appearance/disappearance of CP2, entering/leaving the circle $\sigma_1^2 + \sigma_3^2 = \sigma_0^2$ in the plane $\sigma_2 = 0$ (on the sphere, two CPs of the second kind bifurcate from/off a critical point of first kind corresponding to a tangency on the plane $\sigma_2 = 0$).

The sequence of bifurcations observed for the Hamiltonian $\tilde{\mathcal{H}}_{int}^{(N_P=3, N_{bk}=4)}$ can now be analyzed using the same geometric method as for the Hamiltonians \mathcal{H}_{int} and $\mathcal{H}_{int}^{(1)}$ (see Fig. 11). The usual ACR states A and B are given by external tangencies between \mathcal{S}_{σ_0} and $\mathcal{C}_{\sigma_0, \mathcal{E}}$, the curves $\mathcal{C}_{\sigma_0, \mathcal{E}}^{(\sigma_2=0)}$ being hyperbola-like in this case as well. The fourth panel corresponds to the bifurcation value where one of the two analytical solutions of Eq. (40) are found, $\sigma_0^{(CP1,2)} = 0.00655611$. Note that the analytical determination of all bifurcation values is due to the simplicity of the model, which leads to analytical expressions for all coefficients. Decreasing the value of σ_0 (fifth panel), the phase portrait exhibits two new periodic orbits P_1 and P_2 . Looking in detail the passage from the fourth to the fifth panels, the bifurcation corresponds to the fact that the green hyperbola $\mathcal{C}_{\sigma_0^{(CP1,2)}, \mathcal{E}}^{(\sigma_2=0)}$, tangent to $\mathcal{S}_{\sigma_0^{(CP1,2)}}^{(\sigma_2=0)}$ at the point P in the fourth panel, splits into two hyperbolas in the fifth panel, one (red dashed) corresponding to an outer tangency yielding the stable fixed point P_2 , and the other (black dashed) corresponding to an inner tangency yielding the unstable fixed point P_1 . Decreasing further the value of σ_0 (6th to 8th panel) the two branches of the hyperbola (black dashed) yielding the tangency at P_1 come closer and closer, until they merge at a bifurcation of a ‘CP2’ type ($\sigma_0^{(CP2,1)} = 0.00623676$). Decreasing further σ_0 (9th panel) P_1 becomes stable by a pitchfork bifurcation, giving rise to two new unstable fixed points (CP2) F_1 and F_2 . For still smaller σ_0 (10th and 11th panel) the fixed points F_1 and F_2 move away from the fixed point P_1 , eventually colliding with the B mode (12th panel). This terminates the

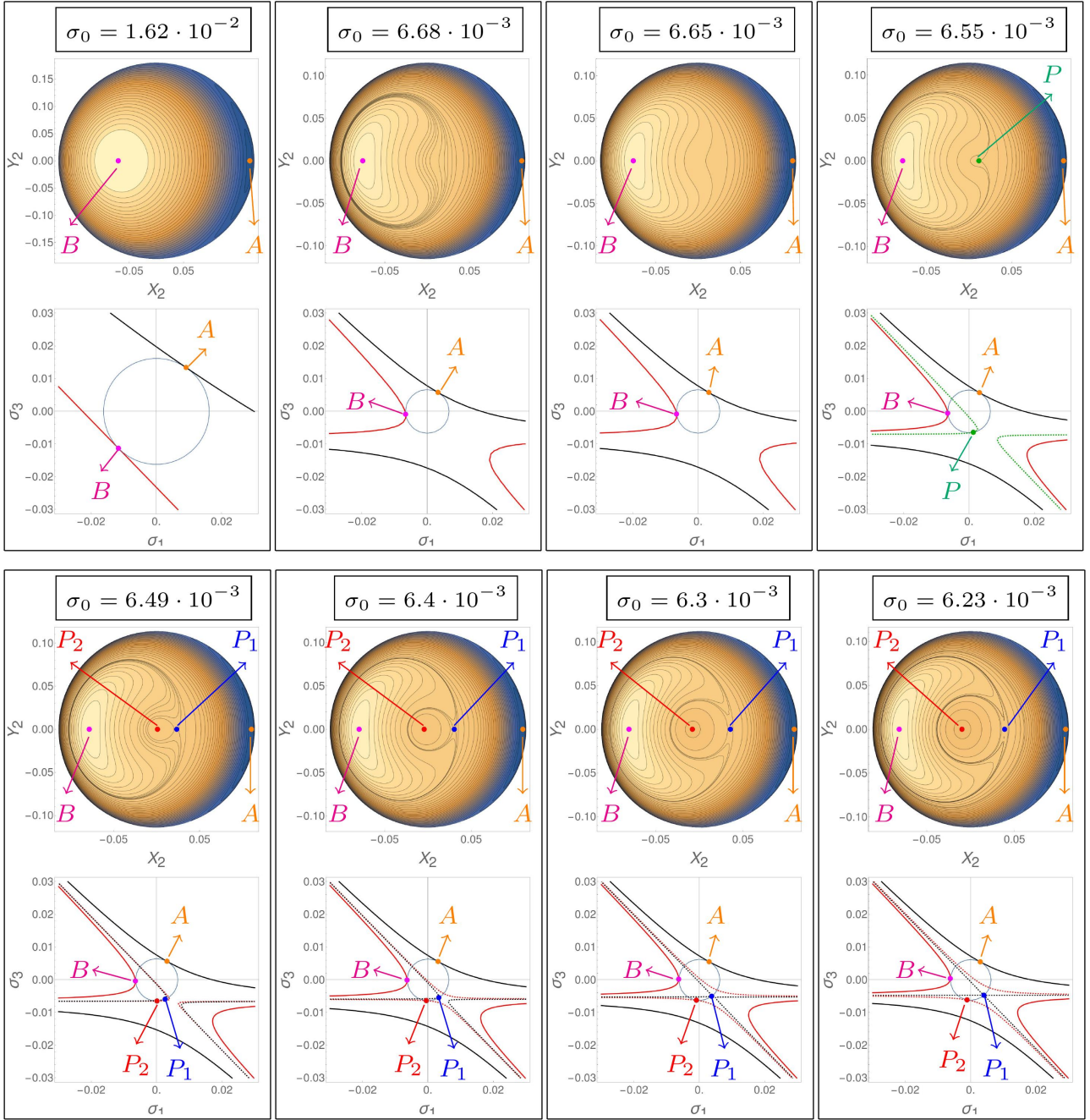


Figure 11: Phase portraits and analysis of the bifurcations (see text), same as in Figure 8, but for the Hamiltonian $\tilde{\mathcal{H}}_{int}^{(N_P=3, N_{bk}=4)}$.

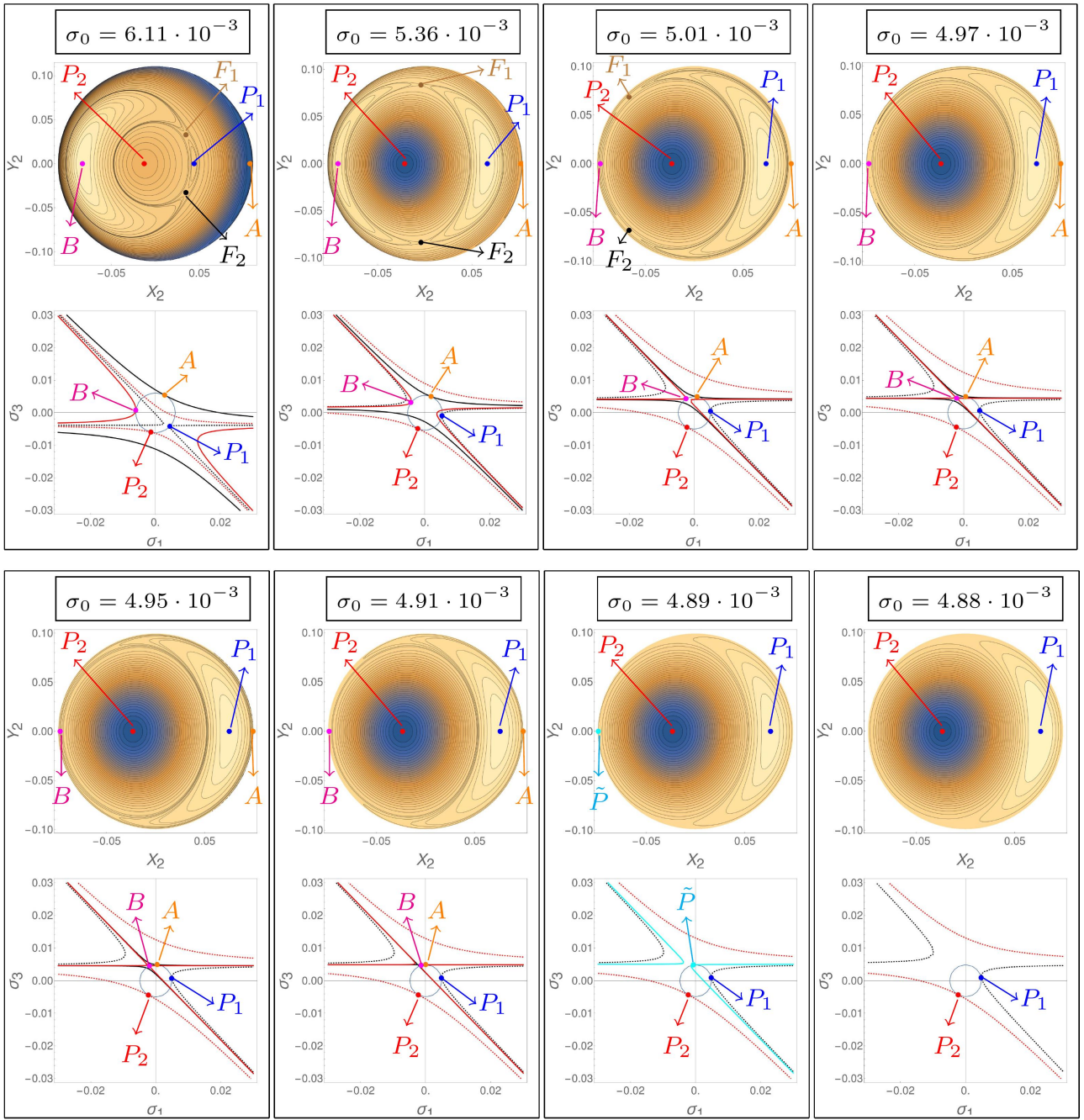


Figure 11: Continued

F -family of periodic orbits by an inverse pitchfork bifurcation which renders the point B unstable, at a value $\sigma_0 = \sigma_0^{(CP2,2)} = 0.00497142$ which, again, can be computed analytically through Eq. (41)). Finally, at still smaller σ_0 (13th panel), mode B becomes unstable (internal tangency), while, as σ_0 decreases, the hyperbolas passing through the tangencies at B and A (red and black in the 13th and 14th panels) approach each other and eventually collide to a single hyperbola (15th panel, cyan) at $\sigma_0 = \sigma_0^{(CP1,1)} = 4.89 \cdot 10^{-3}$, computed also analytically. At the collision the points A and B collide to a single bifurcation point \tilde{P} . Then, for $\sigma_0 < \sigma_0^{(CP1,1)}$ the number of tangency points passes from four to two, i.e., the only stable points surviving at the end of the bifurcation sequence are P_2 and P_1 .

5 Conclusions

In the present paper, we applied the geometric reduction method of [2, 7, 12], based on the representation of the phase space in Hopf variables [3, 6, 18], to address a central problem in planetary orbital theory, namely the analysis of all possible bifurcation sequences in the 3D secular planetary three-body problem leading to periodic orbital states other than the apsidal corotation resonances. Our purpose is twofold: i) to establish the efficiency of the method in producing analytical predictions for the emergence of periodic orbits of the system through bifurcations from the ACR states, and ii) to propose a suitable integrable secular normal form model able to qualitatively capture the sequence of bifurcations as observed in the complete (non-integrable) secular Hamiltonian. Our concluding remarks and results are summarized in the following:

- i. Stemming from the definition of the basic invariant objects of the geometric reduction method for a generic Hamiltonian in 1:1 resonance, i.e., the sphere \mathcal{S}_{σ_0} and the energy surface $\mathcal{C}_{\sigma_0, \varepsilon}$ (Section 3), the complete sequence of bifurcations of periodic orbits in the integrable approximation to the Hamiltonian can be recovered simply computing the tangencies or degenerate transverse intersections between the two surfaces \mathcal{S}_{σ_0} and $\mathcal{C}_{\sigma_0, \varepsilon}$. In particular, depending on the three-body model's numerical parameters, the surface $\mathcal{C}_{\sigma_0, \varepsilon}$ can be either an elliptic cylinder, or a set of two hyperboloid sheets. The degenerate limits of these surfaces are curves close to straight lines in the elliptic case, or two intersecting nearly planar surfaces in the hyperbolic case. Depending on the case considered, we are led to substantial differences as regards the resulting sequence of bifurcations, as well as the form and stability of periodic orbits stemming from the A or B-type ACR states. Both saddle-node and pitchfork bifurcations, arising by changing a control parameter physically equivalent to the mutual inclination between the planetary orbits, can be interpreted by the above geometric representation.
- ii. Section 4 focuses on a comparison of the bifurcation sequences found in various levels of integrable Hamiltonian approximation to the full secular Hamiltonian \mathcal{H}_{sec} of the planetary three body problem. A main conclusion is that considering just \mathcal{H}_{int} , i.e., the integrable part of \mathcal{H}_{sec} , leads to a sequence of bifurcations at variance to the one observed by the phase portraits of the complete secular Hamiltonian \mathcal{H}_{sec} . However, using a 'book-keeping' method in conjunction with normalization by Lie series, we arrive at a secular normal form model $\mathcal{H}_{int}^{(1)}$, which is able to qualitatively reproduce the same sequence of bifurcations as in the complete system.
- iii. A special case of the previous analysis is the one of the octupolar approximation to the Hamiltonian truncated at order 4 in the orbital eccentricities (Subsection 4.3). Computing a secular

normal form as above for this last model leads to the Hamiltonian $\tilde{\mathcal{H}}_{int}^{(N_P=3, N_{bk}=4)}$, for which the bifurcation limits throughout the whole bifurcation sequence can be predicted analytically using the formulas of subsection 3.4. This is particularly useful in cases of so-called hierarchical systems (see, for example, [14], [5] and [16]) where the octupolar expansion is sufficiently precise.

As a final remark, we emphasize that the method here discussed is generic, i.e., applicable to any integrable Hamiltonian model which admits σ_0 (the total angular momentum) as a second integral and approximates the Jacobi-reduced 3D secular planetary dynamics. As regards the ability to provide explicit formulas for the critical bifurcation values of the periodic orbits of the system, this is only limited by the complexity of the formulas arising as higher order truncations are considered of the initial secular Hamiltonian. Thus, in cases of hierarchical systems, where a low order truncation of the Hamiltonian model is sufficiently precise, explicit formulas are easy to provide. In non-hierarchical systems, on the other hand, predictions by the method retain essentially their analytical character, the numerical operations to be performed being limited to computing the sign-definiteness of some suitably defined quadratic forms, as well as root-finding applied to the equations defining the tangencies (points CP1) or transverse degenerate intersections (points CP2) between the surfaces \mathcal{S}_{σ_0} and $\mathcal{C}_{\sigma_0, \mathcal{E}}$.

Acknowledgments: G.P. acknowledges the support of INFN (Sezione di Roma2) and of GNFM/INdAM.

References

- [1] C. Beaugé, S. Ferraz-Mello, and T. Michtchenko. Extrasolar planets in mean-motion resonance: apses alignment and asymmetric stationary solutions. *The Astrophysical Journal*, 593(2):1124–1133, 2003.
- [2] D. Carrasco, J. F. Palacián, C. Vidal, J. Vidarte, and P. Yanguas. Dynamics of axially symmetric perturbed Hamiltonians in 1:1:1 resonance. *Journal of Nonlinear Sciences*, 28:1293–1359, 2018.
- [3] R. H. Cushman and L. M. Bates. *Global aspects of classical integrable systems*, volume 94. Springer, 1997.
- [4] C. Efthymiopoulos. Canonical perturbation theory; stability and diffusion in Hamiltonian systems: applications in dynamical astronomy. In *Workshop series of the asociacion argentina de astronomia*, volume 3, pages 3–146, 2012.
- [5] E. B. Ford, B. Kozinsky, and F. A. Rasio. Secular evolution of hierarchical triple star systems. *The Astrophysical Journal*, 535(1):385–401, 2000.
- [6] H. Hansmann and I. Hoveijn. The 1:1 resonance in Hamiltonian systems. *Journal of Differential Equations*, 266(11):6963–6984, 2019.
- [7] M. Kummer. On resonant non linearly coupled oscillators with two equal frequencies. *Communications in Mathematical Physics*, 48:53–79, 1976.
- [8] J. L. Lagrange. *Essai sur le problème des trois corps*. Mémoires de l’Académie Royale des Sciences de Paris, 1772.

- [9] P. S. Laplace. *Traité de mécanique céleste*. 1798. In *Oeuvres Complètes T.I.*, Gauthier-Villars, 1878.
- [10] G. Laughlin, J. Chambers, and D. Fischer. A dynamical analysis of the 47 Ursae Majoris planetary system. *The Astrophysical Journal*, 579(1):455–467, 2002.
- [11] M. H. Lee and S. Peale. Secular evolution of hierarchical planetary systems. *The Astrophysical Journal*, 592(2):1201–1216, 2003.
- [12] A. Marchesiello and G. Pucacco. Bifurcation sequences in the symmetric 1:1 Hamiltonian resonance. *International Journal of Bifurcation and Chaos*, 26(04):1630011, 2016.
- [13] R. Mastroianni and C. Efthymiopoulos. The phase-space architecture in extrasolar systems with two planets in orbits of high mutual inclination. *Celestial Mechanics and Dynamical Astronomy*, 135(3):22, 2023.
- [14] C. Migaszewski and K. Goździewski. The non-resonant, relativistic dynamics of circumbinary planets. *Monthly Notices of the Royal Astronomical Society*, 411(1):565–583, 2011.
- [15] S. Naoz. The eccentric Kozai-Lidov effect and its applications. *Annual Review of Astronomy and Astrophysics*, 54:441–489, 2016.
- [16] S. Naoz, W. M. Farr, Y. Lithwick, F. A. Rasio, and J. Teyssandier. Secular dynamics in hierarchical three-body systems. *Monthly Notices of the Royal Astronomical Society*, 431(3):2155–2171, 2013.
- [17] H. Poincaré. *Les méthodes nouvelles de la mécanique céleste*. Gauthier-Villars, 1892.
- [18] J. C. van der Meer. Generic one-parameter versal unfoldings of symmetric Hamiltonian systems in 1:1 resonance. *International Journal of Pure and Applied Mathematics*, 53(4):547–561, 2009.